学位論文 （要約）

Development and validation of a cell-based optimally accurate method for computation of synthetic seismograms for arbitrarily heterogeneous and anisotropic Earth models

−Application to spherical coordinates

（セルに基づく最適演算子を用いた任意な不均質媒体における地震波形計算手法の開発、検証、及び球座標系への拡張）

平成２８年１２月博士（理学）申請

東京大学大学院理学系研究科

地球惑星科学専攻

長谷川　慶

波騒は世の常である。
波にまかせて、泳ぎ上手に、雑魚は歌い雑魚は躍る。けれど、誰か知ろう、
百尺下の水の心を。水のふかさを。

吉川英治『宮本武蔵』

PhD Thesis

Development and validation of a cell-based optimally accurate method for computation of synthetic seismograms for arbitrarily heterogeneous and anisotropic Earth models
−Application to spherical coordinates

Kei Hasegawa

Department of Earth and Planetary Science,

Graduate School of Science, University of Tokyo

December 2016

Abstract

Methods for accurate and efficient computation of synthetic seismograms in highly heterogeneous, anisotropic three-dimensional (3-D) models are essential for progress in seismology. Presently available computational methods have greatly contributed to research on inferring large scale 3-D Earth structure, but are not fully satisfactory for use in forward and inverse studies of fine scale 3-D Earth structure, because (i) most methods require great effort in setting up the computational mesh along internal boundaries and irregular surface topography; (ii) such irregular grids degrade computational accuracy; and (iii) higher-order methods are well suited for application to large scale heterogeneous models, but not to fine scale heterogeneous models. To make it possible to accurately and efficiently compute synthetic seismograms for arbitrarily anisotropic and heterogeneous fine scale 3-D models, we develop new methods which we call the "cell-based optimally accurate method (C-OPT)" for Cartesian and the "cell-based spherical optimally accurate method (CS-OPT)" for spherical coordinates. In deriving CS-OPT we use a Jacobian transformation of the weak-form of the equation of motion in order to avoid significant additional computational costs. We present several numerical examples of applications of C-OPT and CS-OPT. We confirm their validity by stability and dispersion analyses, including an analytic derivation of the stability limit of a predictor-corrector scheme of for a 2-D infinite, homogeneous, isotropic case. We show that the numerical dispersion of C-OPT is two more order smaller than that of a conventional finite-difference

scheme. We also compare the accuracy of the synthetic seismograms computed by C-OPT for 2-D media with those computed using the spectral element method (SEM), which is presently one of the most widely used numerical methods. The performance of C-OPT is better than SEM for fine scale heterogeneous media. These results are also expected to hold for a comparison of CS-OPT to SEM in spherical coordinates.

Acknowledgements

I would like to express my profound gratitude to my advisor, Dr. Robert J. Geller for his guidance, support, and encouragement during the doctoral course. He taught me responsibilities as a researcher. I have been very proud to work with him. I thank the other co-workers, Drs. Hiromitsu Mizutani and Nobuyasu Hirabayashi for providing valuable discussions and encouragement. I appreciate the review of my Ph.D. thesis by Drs. Nozomu Takeuchi, Kenji Kawai, Takao Ohminato, Takashi Furumura, Kazuki Koketsu, in particular, provided valuable discussions and comments. I thank members of Geller and Kawai's lab, Mr. Anselme Borgeaud, Mr. Yuki Suzuki, and Ms. Lina Yamaya, for their helpful advice and encouragement. I also thank alumni of Geller's lab, especially Drs. Nozomu Takeuchi, Hiromitsu Mizutani, Kenji Kawai, Nobuaki Fuji, Kensuke Konishi, and Mr. Mitsutsugu Igarashi, for their remarkable comments and aspiring guidance. Some parts of this research were supported by grants from Schlumberger K.K.

I thank members of the "Whole Solid Earth Colloquium", Drs. Nobumasa Funamori, Ataru Sakuraba, Satoru Honda, Atsuko Namiki, Keisuke Nishida, Naofumi Aso, and Daisuke Wakabayashi, for their insightful comments and precious support. I also thank all members of Solid Earth Science Group, especially Drs. Satoshi Ide, Ryosuke Ando, and Tsuyoshi Iizuka for their fruitful advice. I also thank all staffs of the office of the Department of the Earth and Planetary Science, especially Ms. Megumi Mikamoto, Mamiko Hamada and Rika Yoshiyama for daily support and

encouragement. I also thank all staffs of the secretarial office of the Solid Earth Science Group, Ms. Yukako Baba, Ms. Ayako Fukuda, and Ms. Sumiko Kakizawa for daily support and encouragement.

I thank members of Earthquake Research Institute, especially Drs. Hitoshi Kawakatsu, Kazuki Koketsu, Takashi Furumura, Nozomu Takeuchi, Takao Ohminato, Tsuyoshi Ichimura, Takuto Maeda, and Akiko Takeo for providing valuable discussions and encouragement. I also thank researchers outside of the University of Tokyo, especially Drs. Li Zhao, Akiko To, Yann Capdeville, Atsunari Konishi, Toshio Nagashima, and Takashi Nakagawa for their encouragement.

I had nice days with members working in room 712 of Science Bldg. 1 and the guys who frequently visit in the room, Drs. Ataru Sakuraba, Hiromitsu Mizutani, Kosuke Naemura, Kazuaki Ohta, Kensuke Konishi, Koki Idehara, Kota Okamoto, Mr. Shintaro Tamura, Yoshiharu Kurihara, Satoshi Ogino, Shimon Abe, Anselme Borgeaud, Yuki Maehara, Shuntaro Kanamori, and Ms. Miki Aso.

I deeply thank my father Junichi, my mother Tomoko, and my grandmother Yasuko for their support, encouragement, and patience. I also thank my brothers, Shunji, Yosuke, and Tsuyoshi for encouragement. I also thank my relatives, Mitsuhashis, Akamas, and Takis for encouragement.

I was healed every day during the last two years of my doctoral course by a lot of stray cats living near my apartment, I call them as Shiro, Mannaka, Boss, Shitataka, Sabi, Chatora, Saba, Taro, Shinkeishitsu, Kinako, Debu, Kurochibi, Ponchan, Chibi, Heart, Tado, and Michans.

I deeply thank Ms. Aoi Matsuyama for encouraging me to enter the graduate

school. I deeply thank Ms. Mariko Ueno for her daily support and encouragement. I deeply thank my fiancée Saaya for her love. Finally, I deeply thank my late mother Shouko for her love. She lives forever in my heart.

Contents

Chapter 1

General Introduction

Seismograms contain vital information about rupture process of earthquakes (e.g. Guo *et al.* 2013), mechanisms of volcanic eruptions (e.g. Ohminato *et al.* 2006), and the interior structure of the Earth (e.g. Takeuchi 2007; Kawai *et al.* 2014; French & Romanowicz 2015). Joining seismic analysis to knowledge of other fields of study such as mineral physics, we have succeeded to reveal dynamic systems of the Earth (e.g. Kawai & Tsuchiya 2009; Namiki *et al.* 2013). Presently, accurate reproduction of seismograms under assumed source and structure models becomes a critical step for highly-detailed seismic analysis. However, although there have been many sophisticated methods, this step for general complex models has been still a challenging work. In this thesis, we present a new method having potential to enable efficient and accurate computation of synthetic seismograms for such complex media.

In this chapter, we review historical development of studies for methods for computation of synthetic seismograms and their applications in Section 1.1, and see

missing points in previous studies from the author's point of view in Sections 1.2 and 1.3. Then we give the purpose of this thesis in Section 1.4. Finally, we give an overview of this thesis in Section 1.5.

1.1 Numerical methods and their applications in seismology

In the past decades from the 1970s, most programs of seismology are focused on stratified media. Many methods specialized to compute synthetic seismograms for such media have been presented. Notable examples are the reflectivity method (e.g. Fuchs & Müller 1971; Kennett 1983), the modal superposition approach (e.g. Gilbert 1970; Woodhouse 1988), and the direct solution method (DSM; Geller & Ohminato 1994). The reflectivity method and the modal superposition approach are, respectively, well-suited to compute body-waves at high frequencies and surface-waves at low frequencies, and applied to several studies (e.g. Lay & Helmberger 1983; Grand & Helmberger 1984; Ishi & Tromp 1999). But, for more general purposes dealing with broad-band frequencies, DSM is well-suited to compute complete synthetic seismograms including body-waves and surface-waves.

In DSM for global Earth's problems, the displacement is decomposed by vector spherical harmonics, and then the partial differential equations for the expansion coefficients are directly computed by solving a system of linear equations. (e.g. Cummins *et al.* 1994ab). Further, DSM improved its efficiency and accuracy by using the modified operators of the optimally accurate method (OPT; Geller

& Takeuchi 1995 cited as GT95 below). Presently, DSM-software is a promising method for efficient and accurate computation of complete synthetic seismograms for laterally homogeneous structures (Kawai *et al.* 2006). Using DSM and efficient algorithms for computation of partial derivatives for model parameters (Geller & Hara 1993), full-waveform inversions have been extensively conducted to estimate 3-D models of the S-velocity structure of the whole mantle (Takeuchi 2007), fine scale 1-D models of the S-velocity structure of the lowermost mantle (Kawai *et al.* 2007ab, 2009, 2010; Kawai & Geller 2010abc; Konishi *et al.* 2009, 2012), and fine scale 1-D models of the S-velocity and Q structures of the mantle transition zone (Fuji *et al.* 2010). Recently, the inversion method is extended for estimation of fine scale 3-D S-velocity models, and applied for the lowermost mantle (Kawai *et al.* 2014; Konishi *et al.* 2014; Suzuki *et al.* 2016).

For 2-D and 3-D heterogeneous media, full-numerical methods, in which the time and the space are fully discretized, will be preferable, and many methods have been presented. These methods basically can be classified by two formulations constructing their basis: the strong and weak forms of the equation of motion (see Strang & Fix 1973 for their difference). Notable examples for strong form-based methods include the finite-difference method (FDM; Altherman & Karal 1968; Boore 1970; Kelly *et al.* 1976, Virieux 1984, 1986; Korn 1987; Levander 1988; Igel *et al.* 1995; Ohminato & Chouet 1997) and the pseudo-spectral method (PSM; Furumura *et al.* 1998ab). Notable examples for weak form-based methods include the conventinal finite-element method (FEM; Mullen & Belytschko 1982; Marfurt 1984; Bao *et al.* 1998; Zhang & Verschuur 2002; Koketsu *et al.* 2004), the discontinuous Galerkin

method (Käser & Dumber 2006), the Chebyshev FEM (Seriani & Priolo 1994), and the spectral element method (SEM; Patera 1984; Komatitsch & Vilotte 1998; Komatitsch & Tromp 1999; Komatitsch *et al.* 2000ab). Besides, a sophisticated reflectivity method for irregularly layered structures (Koketsu 1987; Koketsu *et al.* 1991), and a method based on a modified scattering theory (Wu & Zheng 2014) are also notable methods suitable for relatively simple heterogeneous structures. Hybrid methods between full-numerical and semi-analytical methods are also presented for 3-D regionally heterogeneous problems (Zahradník & Moczo 1996; Wen & Helmberger 1998; Capdeville *et al.* 2003ab; Montellier *et al.* 2013).

On the author's knowledge, FDM was first introduced for seismic wave analysis by Altherman & Karal (1968). Boore (1970) and Kelly *et al.* (1976) are also notable early researches to apply FDM to reproduce seismograms for 2-D heterogeneous media. The above studies used the collocated grid with the displacement formulation of the equation of motion, but to improve accuracy and efficiency, especially for heterogeneous media and higher P/S-velocity ratio, the staggered-grid with the velocity-stress formulation was introduced by Virieux (1984, 1986). The staggered-grid method can efficiently implement any heterogeneous isotropic media, and relatively easily implement any topography of free surface (Ohminato & Chouet 1997). To improve further accuracy, higher-order staggered-grid method have been presented (e.g. Levander 1988 for the 4th-order scheme). Since FDM is one of the simplest methods and can easily input complex structures, presently the staggered-grid FDM had great success especially in regional scale problems (e.g. Furumura, T. & Kennett, B. L. N 2008). However, as mentioned by Igel (2016),

it is difficult to extend to general anisotropic media, or needs interpolations which can degrade the accuracy (Igel *et al.* 1995). Although there need additional computational costs to compute geometrical terms for spherical coordinates compared to the cartesian case, several studies have been presented for spherical problems (Igel & Weber 1995, 1996; Igel 1999; Igel *et al.* 2002; Jahnke *et al.* 2008; Zhang *et al.* 2012).

PSM is a dispersionless method, and can handle general anisotropic media in a straightforward manner, but ill-suited for parallel computation, and presently there are few studies to apply it to realistic 3-D problems.

Recently, FEM begins to widely used for seismology since it can express topography of free surface and internal discontinuities by using mesh deformations. Lower-order FEMs are frequently used for simulation of seismic ground motion for hazard prediction (e.g. Hori *et al.* 2016) due to its usability. For global seismology, higher-order FEMs are preferable to many seismologists because of low numerical dispersion properties. Among them, SEM is one of the most prominent methods because the mass matrix is diagonal and thus we can easily compute its inverse matrix, which enable direct computation of the displacement at each time step. Notable studies for SEM for spherical problems include Komatitsch & Tromp (2002ab), Capdeville *et al.* (2003ab), and Cupillard *et al.* (2012), and notable studies for their applications include To *et al.* (2011) for a modeling of an ultra-low velocity zone on the core-mantle boundary beneath Hawaii, and Fichtner *et al.* (2009ab; 2013) for full-waveform inversions for crust and mantle structures of Eurasian and Oceanian regions.

Although SEM had great success in studies to reveal large-scale global Earth's structures, there are also some disadvantages compared to lower-order FEM in practical applications: (i) it requires relatively larger computational costs than lower-order methods of the same grid points since the bandwidth of the stiffness matrix is relatively larger; (ii) it requires to consider strong deformation of elements in order to align with discontinuities of a structure because SEM uses considerably larger elements compared to lower-order FEM cases. Recently, Capdeville & Marigo (2007) and Capdeville & Cance (2015) developed a method to derive a smoothed structure against an original structure including many complex discontinuities, which will enable to compete the equivalent seismograms to for the original structure without the efforts of a mesh-generation. Further, to overcome larger computational costs, SEM software-developers have taken full advantage of sophisticated computational architecture such as GPU-computing (Komatitsch *et al.* 2010).

However, applications for 3-D fine scale heterogeneous structures such as laminated crustal models (e.g. Champion *et al.* 2006), scattering crust/mantle models (e.g. Furumura & Kennett 2008), and D$''$ models (e.g. Kawai *et al.* 2014; To *et al.* 2005, 2012) may have been still challenging works. Our method presented in this thesis, which we call "cell-based optimally accurate method (C-OPT)", will be suited to computation of synthetic seismograms for such models. C-OPT is based on the weak form of the equation of motion, because this formulation can easily set up the boundary conditions for free surfaces and fluid-solid interfaces. In that respect, C-OPT may be categorized into a lower-order scheme of FEM rather than FDM. But similarly to FDM, in C-OPT the structure models are represented by

regularly spaced cells (voxels), without requiring special gridding to match internal discontinuities. Consequently, the topography of free surface and internal discontinuities is approximated as staircases. Although the accuracy might be somewhat degraded by the staircase approximation, this makes it much easier to conduct simulations for complex structures than methods which require special grid generation for each model. To improve the accuracy, C-OPT uses original interpolations and differential operators to optimize the net error of synthetic seismograms. As a result, C-OPT has comparable accuracy as schemes having 4th-order accuracy without significantly increasing computational costs. Furthermore, for spherical coordinates we present a new method based on C-OPT, which we call "cell-based spherical optimally accurate method (CS-OPT)".

1.2 Error analysis for numerical methods

A method for stability and dispersion analysis was developed by von Neumann & Richtmyer (1950), where they derived an upper limit of the temporal interval versus a given spatial interval for a particular scheme by substituting a harmonic ansatz into the scheme. Their interest was originally for the stability condition, but presently their method has been also frequently used for numerical dispersion analysis. Related to their work, Geller & Takeuchi (1998 cited as GT98 below) and Geller *et al.* (2012 cited as GMH12 below) developed general frameworks for stability analysis, but now we omit the detail (see Chapter 4 for detailed review). Numerical dispersion is an artificial phenomenon which causes changes of the phase velocities of P and S-waves depending on their wavelength and propagation direc-

tions, and can occur even when the medium is isotropic and homogeneous. Since the travel-times of P and S-waves are critical informations in seismology, suppressing numerical dispersion is one of the most important criteria for setting up spatial and temporal grid size of a particular scheme depending on desirable accuracy (needless to say, in the extent satisfying the stability condition).

There have been many studies for dispersion analysis. Mullen & Belytschko (1982) conducted the dispersion analysis for the conventional lower-order FEM. Marfurt (1984) suppressed the numerical dispersion of the lowest-order FEM by numerically blending consistent and lumped mass matrices. Cohen (2002) showed the dispersion analysis for many higher-order methods including SEM for the scalar wave equation. For the elastic cases, De Basabe & Sen (2007) and Seriani & Oliveira (2008ab) conducted the dispersion analysis for SEM. De Basabe & Sen (2010) studied effects of several time integration methods on the numerical dispersion of SEM. Unanimously, their results show the prominent superiority of higher-order methods including SEM.

However, although most error analyses emphasized dispersion analysis, small dispersion does not necessarily guarantee the accuracy of synthetic seismograms. Related to this controversy, Hasegawa *et al.* (2016) found existence of previously unrecognized type of error in higher-order finite element methods (ho-FEMs) including SEM, which is also shown in Appendix A. Moczo *et al.* (2011) is another notable work to analyze the numerical error from different aspects.

Finally, regarding SEM, it can avoid strong error caused by discontinuities of the structures by using deformed mesh aligning with the discontinuities. However, the

mesh of SEM composes nested elements, where each element contains many grid points. Consequently, the size of elements will be considerably larger than lower-order FEMs of the same grid points. Then SEM requires strong deformation of the mesh in order to align with discontinuities. Therefore, effects of such deformation on the accuracy should also be considered. Oliveira & Seriani (2011) estimated such effects by the dispersion analysis. But their interest is only for the scalar wave equation. In Appendix B, we extend their analysis to the case of the elastic wave equation, and we see a notable remark.

1.3 Previous works for optimally accurate method (OPT)

GT95 developed a general error analysis for the error of synthetic seismograms based on the perturbation theory and modal expansion for the numerical solution. Then they derived the criterion of optimal accuracy, and modified operators satisfying the criterion for the frequency-domain of the weak-form of the equation of motion for horizontally homogeneous isotropic media. These operators have been applied to DSM for computations of synthetic seismograms and their partial derivatives for global Earth models (Takeuchi *et al.* 1996 for laterally homogeneous and isotropic cases; Cummins *et al.* 1997 for axisymmetric heterogeneous and isotropic cases; Takeuchi *et al.* 2000 for weakly heterogeneous and isotropic cases; Kawai *et al.* 2006 for laterally homogeneous and transversely isotropic cases). Related to these works, Takeuchi & Geller (2003) developed an accurate representation of the source term of

OPT when the source is located at an arbitrary point between the grid points, and was implemented by Kawai *et al.* (2006). As mentioned in Section 1.1, presently DSM-software has been widely used by many other researchers as well as our group for studies of full-waveform inversions and forward modelings.

However, for more general purposes including computation of synthetic seismograms for arbitrarily 3-D heterogeneous structures, the time-domain scheme of OPT is highly desirable. GT98 developed modified FDM operators satisfying the criterion of optimal accuracy for 1-D acoustic media, where they first derived the time-domain implicit scheme, and then derived the predictor-corrector (P-C) scheme by separating the implicit scheme into the zeroth-order and the first-order terms in order to enable two-step explicit computations. Mizutani *et al.* (2000) showed that P-C scheme of GT98 is essentially equivalent to Lax & Wendroff (1964) except for small difference of implementation of source term. Takeuchi & Geller (2000 cited as TG00 below) extended GT98 for 2-D and 3-D isotropic elastic media.

Regarding the accuracy of OPT, Mizutani *et al.* (2000) showed that although PSM is most likely suitable for homogeneous cases, OPT shows better accuracy than PSM for some heterogeneous cases. This work showed only for 1-D cases, and considered for PSM. However, such a tendency might also hold for other higher-order methods such as SEM; i.e., although higher-order methods are preferable to homogeneous or large scale heterogeneous structures, these might be inaccurate for fine scale heterogeneous structures. In contrast, although OPT might not have prominent accuracy for homogeneous or large scale heterogeneous structures compared to higher-order methods, OPT might have relatively robust accuracy even

for fine scale heterogeneous structures. In other words, our inference is as follows. Higher-order methods achieve their accuracy by minimizing the error of the numerical operators themselves. Consequently, their numerical operators require relatively wide range of the footprints to compute the differentiation terms. Then higher-order approximations might break down when there exists heterogeneity in the footprints of the numerical operators. In contrast, OPT is designed to minimizes the error of the numerical solution itself, but not the numerical operators themselves. Thus, it uses relatively narrow range of the footprints of the numerical operators, and such problem might not occur.

Although OPT has potential noted above, there has been a limitation in TG00: our group found that there exist situations of instability of computation in TG00 unless spacial treatment is put on the free surface boundary condition. It is due to presence of a negative eigenvalue of the stiffness matrix of TG00 in such situations. To avoid such unstable situations, Geller *et al.* (2013ab cited as GMHT13 below) recently developed the basic concept of C-OPT, which is a reformulated version of OPT. In C-OPT, the whole volume is divided into cells to approximately compute the integrals of the weak formulation, and in each cell, the sampling point of the integration is put at the center of a cell. As shown in Chapter 2, the cell-based formulation invariably guarantees nonnegative-definiteness of the stiffness matrix. For efficient time integrations, GMH12 developed a modified P-C scheme which is well-suited to C-OPT. However, although GMHT13 succeed to define the stiffness matrix of C-OPT, they provisionally used the mass matrix of TG00.

In this thesis, we construct a complete form of C-OPT including fluid-solid cou-

pling cases as well as the mass matrix. Then we extend C-OPT to CS-OPT for spherical problems. Furthermore, the inference mentioned above on different behavior of accuracy between OPT and higher-order methods is confirmed in Chapter 5, where we compare accuracy of C-OPT with SEM for several 2-D vertically heterogeneous models.

1.4 Purpose of this thesis

In Section 1.1, we reviewed resent progress of numerical methods and their applications, and introduced C-OPT and CS-OPT presented in this thesis. In Section 1.2, we reviewed error analysis of numerical methods especially for SEM, in which we introduce the motivation for studies shown in the appendices of this thesis. In Section 1.3, we reviewed the current situation for previous situation of studies for OPT and see potential of OPT and difficulties in the pervious studies of OPT.

In this thesis, we establish fundamental theory of C-OPT for cartesian coordinates, and CS-OPT for spherical coordinates. These methods are applicable to arbitrary anisotropic and heterogeneous 3-D media including fluid-solid coupling media. CS-OPT is well-suited to compute synthetic tele-seismic body-waves propagating global models of the Earth. As mentioned in Section 1.3, it is the first time to show a complete form of C-OPT which is applicable to general anisotropic fluid-solid coupling 3-D media. Extension to spherical coordinates (CS-OPT) also previously has not been presented. Derivations of stability condition and dispersion properties of C-OPT (and CS-OPT) are also important topics in this thesis.

It is also important to reveal superior and inferior aspects of C-OPT (and CS-

OPT) compared to previously developed other methods. In this thesis we focus on SEM because it is not only one of the most prominent methods, but also can be a representative method for higher-order methods. For this purpose, we conduct comparison of accuracy of C-OPT and SEM for homogeneous and vertically heterogeneous models. Although, we consider only simple 2-D structures due to limitation of computational resources, our results are consistent and systematic, and thus these features will hold for general 3-D spherical cases. Therefore, here we may show sufficient potential of C-OPT and CS-OPT by this study.

Finally, related to the above studies, we find several new remarks for accuracy of SEM which previously have not been recognized. These results will contribute to criterions for mesh-generation as well as comparison studies for SEM. Note that these will be intrinsic features only for SEM and most other ho-FEMs, and not for C-OPT (and CS-OPT). Although, these topics may not be directly related to the above works for C-OPT, these can be supplemental results to compare C-OPT with SEM, and thus we show them in the appendices of this thesis.

1.5 Overview of this thesis

This thesis is organized as follows:

Chapter 2: We show the theory of C-OPT. Some parts of C-OPT previously have been presented by GMHT13. But here we show a complete form of C-OPT, especially derivation of the mass matrix and the fluid-solid boundary operators.

Chapter 3: We derive CS-OPT. We also show several numerical examples for applications of CS-OPT.

Chapter 4: We conduct stability and dispersion analysis of P-C scheme of C-OPT for the cases of the 2-D infinite, isotropic, homogeneous media.

Chapter 5: We compare accuracy of synthetic seismograms of C-OPT with SEM for 2-D homogeneous and heterogeneous models.

Chapter 6: We mention the reaching points in this thesis, and future works

Appendix A: We conduct a general error analysis for ho-FEMs including SEM, and show existence of previously unrecognized type of error in such methods. A significant portion of this chapter was published in *Geophysical Journal International* (2016, vol. 205, 1532–1547).

Appendix B: We study effects of grid-deformation on the accuracy of SEM by using a new method of dispersion analysis which can be applicable to deformed grids.

Chapter 2

本章（15 から 56 ページ）については、5 年以内に雑誌等で刊行予定のため、非公開。

Chapter 3

本章（57 から 75 ページ）については、5 年以内に雑誌等で刊行予定のため、非公開。

Chapter 4

本章（76 から 92 ページ）については、5 年以内に雑誌等で刊行予定のため、非公開。

Chapter 5

本章(93 から 105 ページ)については、5 年以内に雑誌等で刊行予定のため、非公開。

Chapter 6

Conclusion

In this thesis, we established theoretical bases of a cell-based optimally accurate method (C-OPT) for accurate and efficient computations of synthetic seismograms for arbitrarily anisotropic and heterogeneous 3-D media including fluid-solid coupling cases. For C-OPT, the structure models are represented by regularly spaced cells (voxels), without requiring special gridding to match internal discontinuities. This makes it much easier to conduct simulations for complex structures with irregular internal boundaries than methods which require special grid generation for each model. The numerical operators of C-OPT are designed to satisfy the criterion for optimal accuracy of Geller & Takeuchi (1995; note that abbreviated citations such as GT95 are not used in this chapter, in order to make it self-contained), which enables accurate and efficient computation of synthetic seismograms.

For global scale Earth's models including lateral heterogeneity and anisotropy, we next extended these results by deriving a new method for spherical coordinates, which we call a cell-based spherical optimally accurate method (CS-OPT). Although

this thesis dose not present softwares of C-OPT and CS-OPT optimized to practical applications such as full-waveform inversions, our performance studies suggest they will be promising methods for accurate and efficient computations of synthetic seismograms.

We now summarize the contents of this thesis in more detail. Geller *et al.* 2013ab previously develop the concept of C-OPT and define the stiffness matrix. In Chapter 2, we presented a complete form of C-OPT including a derivation of the mass matrix, and extended C-OPT to be applicable to fluid-solid coupling cases. We also discussed the relation of C-OPT to previous studies of optimally accurate methods, and showed that at inner nodes in a homogeneous medium, the numerical operators for spatial differentiation are equivalent to previous versions of OPT (e.g. Takeuchi & Geller 2000). In this sense C-OPT can be considered to be a reformulation of previous OPT schemes. However, there were some instabilities due to the way the operators for nodes at external boundaries were handled. C-OPT overcome these difficulties.

In Chapter 3, we derived CS-OPT based on C-OPT operators. We showed that by defining equivalent physical parameters for spherical coordinates, we can use the same algorithm as C-OPT without any additional computations. This approach will also be useful especially for schemes based on regular gridding. Although our derivation is based on the weak form of the equation of motion, similar approach may be able to used for strong form-based methods such as FDM. Although, our software is still a prototype, we confirmed its validity by computations of synthetic seismograms using CS-OPT for several Earth's models.

In Chapter 4, we conducted a stability and dispersion analysis of C-OPT. For optimally accurate time integration, C-OPT uses the predictor-corrector (P-C) scheme of Geller *et al.* (2012). For P-C scheme for 2-D infinite, isotropic, homogeneous cases, we analytically derived the stability limit as a function of S-wave to P-wave velocity ratio. We also showed that "a second island of stability" (i.e., two stable regions of the Courant number separated by an unstable region does) not exist for this case. From dispersion analysis of C-OPT, we see that the numerical dispersion of C-OPT is two orders of accuracy better than conventional FDM. This result follows from the results of Geller & Takeuchi (1998) for the 1-D case. Although the stability condition and the numerical dispersion of a particular method are widely considered to be important to assess the validity of the numerical methods, such analyses for P-C schemes for 2-D or 3-D cases had not been yet conducted. Our analysis in Chapter 4 assumes an infinite homogeneous medium; this assumption is commonly used in validation studies for numerical methods (e.g. von Neumann & Richtmyer 1950). Geller & Takeuchi (1998) pointed out the importance of studying stability condition for the case of heterogeneous finite media. Our study is a first step towards such more general results.

In Chapter 5, we conducted a comparison of C-OPT and the spectral element method (SEM) as a reference scheme. C-OPT can be categorized into a lower-order scheme, and SEM is a higher-order scheme which is widely used in seismology. First, we saw that SEM has prominent accuracy in applications to homogeneous and weakly heterogeneous media, but that its accuracy is dependent on the amount and type of the heterogeneity of the model. In particular, the accuracy of SEM

worsens for fine scale heterogeneous models. In contrast, we saw that C-OPT does not have better accuracy than SEM, but the accuracy is relatively robust for both homogeneous and large/fine scale heterogeneous models, even for models including internal discontinuities without any irregular gridding. These results are also expected to hold for CS-OPT for spherical coordinates.

6.1 Future works

In my opinion, one of the most prominent advantages of C-OPT and CS-OPT is that they can be used to conduct simulations for complex structures with irregular internal boundaries without requiring special grid generation for each model. This makes it much easier to input a model structure. Furthermore, we see that C-OPT and CS-OPT provide sufficient and robust accuracy for both homogeneous and heterogeneous models, including models with strong high wavenumber heterogeneity, or/and models with internal discontinuities. Thus, C-OPT and CS-OPT will be suitable to conduct seismic wave simulations especially for complex structures such as crustal models, mantle models with scattering, and heterogeneous D″ models with arbitrary anisotropy. They will be compatible with a full-waveform inversion since we can conduct the inversion using regular gridding for both steps of waveform computations (and their derivatives) and model perturbations.

Towards such practical applications, we have the following issues to be resolved at most: (i) extension to anelastic media; (ii) implementation of a more effective absorbing boundary condition; (iii) code-optimization for large-scale computations; (iv) development of a multigrid scheme for C-OPT.

For (i), we may have to consider a new C-OPT for the memory variable formulation of C-OPT (Kay & Krebes 1999). But it may be sufficient to use C-OPT in this thesis to solve the wave equation at each time step as just same as for the elastic case, and use conventional methods to solve the partial difference equation for the memory-variable tensors, because the numerical dispersion is the most important error in synthetic waveforms, and C-OPT successfully suppresses the numerical dispersion using the minimum bandwidth of matrix operators.

For (ii), it is worth introducing a perfect matched layer for an effective absorbing boundary condition (Komatitsch & Tromp 2003), rather than the most simple formulation of Cerjan *et al.* (1985) used in this thesis. However, we should eliminate possibilities of presence of artifacts or/and unstable situations in the implementation.

For (iii), there are two approaches for the implementation of C-OPT. One is "the element-based implementation", in which we compute the derivatives of the stress tensor by computing them for each cell and time step, and then assemble them. The other is "the global matrix implementation", in which we first define the global stiffness matrix, and then for time step we compute the derivatives of the stress tensor by operating the global stiffness matrix on the displacement at the current time (needless to say, we should make computations only for non-zero elements of the matrix). Although the former approach can be easily implemented, however, the latter approach is preferable due to the low costs of computing extra-intermediate variables. But, its memory usage is less efficient than the former approach despite that the global matrix is sparse. Thus, it depends on a computer architecture.

An optimal implementation for large scale parallel computations will also be an important future work. For this purpose, we should separate the 3-D spatial region so that for each time step the amount of computational costs is nearly equal for each computation-node. Minimizing the amount of data communications between computation-node is also important.

Finally, for (iv), one of the most famous approaches is the mortar method (e.g. Bernardi et al. 1990, 1994), in which for each time step we simply make computations separately for each region in which we use a uniform size of regular mesh, and then connect the displacement along the boundaries of the separated regions with proper boundary conditions. However, this approach can often cause artifacts along the boundaries. Thus, it may be more preferable to develop a cell which connects small and large cells.

References

Ainsworth, M. & Wajid, H. A., 2009. Dispersive and dissipative behavior of the spectral element method, *SIAM J. numer. Anal.*, **47**, 3910–3937.

Alterman, Z. & Karal, F., 1968. Propagation of elastic waves in layered media by finite difference methods, *Bull. seism. Soc. Am.*, **58**, 367–398.

Bao, H., Bielak, J., Ghattas, O., Kallivokas, L. F., O'Hallaron, D. R., Shewchuk, J. R. & Xu, J., 1998. Large-scale simulation of elastic wave propagation in heterogeneous media on parallel computers, *Comp. Meth. Appl. Mech. Eng.*, **152**, 85–102.

Bernardi, C., Debit, N. & Maday, Y., 1990. Coupling finite element and spectral methods: first results, *Math. Comput.*, **54**, 21–39.

Bernardi, C., Maday, Y. & Patera, A. T., 1994. A new nonconforming approach to domain decomposition: the Mortar element method, in *Nonlinear Partial Differential Equations and Their Applications*, eds. Brezis, H. & Lions, J. L., Séminaires du Collége de France, Paris.

Boore, D. M. 1970. Love waves in nonuniform waveguides: finite difference calculations. *J. Geophys. Res.*, **70**, 1512–1527.

Brillouin, L., 1953. *Wave Propagation in Periodic Structures*, 2nd edn., Dover, New York.

Capdeville, Y., Chaljub, E., Vilotte, J. P. & Montagner, J. P., 2003a. Coupling the spectral element method with a modal solution for elastic wave propagation in global earth models, *Geophys. J. Int.*, **152**, 34–67.

Capdeville, Y., Romanowicz, B. & To, A., 2003b. Coupling Spectral Elements and Modes in a spherical earth: an extension to the "sandwich" case. *Geosphys. J. Int.*, **154**, 44–57.

Capdeville, Y. & Marigo, J. J., 2007. Second order homogenization of the elastic wave equation for non-periodic layered media *Geophys. J. Int.*, **170**, 823–838

Capdeville, Y. & Cance, P., 2015. Residual homogenization for elastic wave propagation in complex media. *Geophys. J. Int.*, **200**, 886–999.

Cerjan, C., Kosloff, D., Kosloff, R., & Reshef, M., 1985. A nonreflecting boundary condition for discrete acoustic and elastic wave equations, *Geophysics*, **50**, 705–708.

Champion, M. E. S., White, N. J., Jones, S. M. & Priestley. K. F., 2006. Crustal velocity structure of the British Isles; a comparison of receiver functions and wide-angle seismic data *Geophys. J. Int.*, **166**, 795–813.

Cohen, G., 2002. *Higher-Order Numerical Methods for Transient Wave Equations*, Scientific Computation, Springer-Verlag, Berlin.

Cummins, P. R., Geller, R. J., Hatori, T. & Takeuchi, T., 1994a. DSM complete synthetic seismograms: SH, spherically symmetric, case, *Geophys. Res. Lett.*, **21**, 533–536.

Cummins, P. R., Geller, R. J. & Takeuchi, N., 1994b. DSM complete synthetic seismograms: P-SV, spherically symmetric, case, *Geophys. Res. Lett.*, **21**, 1663–1666.

Cummins, P. R., Geller, R. J. & Takeuchi, N.,1997. Computation of complete synthetic seismograms for laterally heterogeneous models using the Direct Solution Method, *Geophys. J. Int.*, **130**, 1–16.

Cupillard, P., Delavaud, E., Burgos, G., Festa, G., Vilotte J. P., Capdeville, Y., & Montagner, J. P., 2012. RegSEM: a versatile code based on the spectral element method to compute seismic wave propagation at the regional scale, *Geophys. J. Int.*, **188**, 1203–1220

De Basabe, J. D. & Sen, M. K., 2007. Grid dispersion and stability criteria of some common finite-element methods for acoustic and elastic wave equations, *Geophysics*, **72**, T81–T95.

De Basabe, J. D. & Sen, M. K., 2010. Stability of the high-order finite elements for acoustic or elastic wave propagation with high-order time stepping, *Geophys. J. Int.*, **181**, 577–590.

Dziewonski, A. M. & Anderson, D. L., 1981. Preliminary reference Earth model, *Phys. Earth Planet. Inter.*, **25**, 297–356.

Fichtner, A., Igel, H., Bunge, H. P. & Kennett, B. L. N., 2009a. Simulation and inversion of seismic wave propagation on continental scales based on a Spectral-Element Method, *J. Numer. Anal. Ind. appl. Math.*, **4**, 11–22.

Fichtner, A., Kennett, B. L. N., Igel, H. & Bunge, H.-P., 2009b. Full waveform tomography for upper-mantle structure in the Australasian region using adjoint methods, *Geophys. J. Int.*, **179**, 1703–1725.

Fichtner, A., Trampert, J., Cupillard. P., Saygin, E., Taymaz, T., Capdeville, Y. & Villasenor, A., 2013. Multiscale full waveform inversion, *Geophys. J. Int.*, **194**, 534–556.

French, S. W. & Romanowicz, B., 2015. Broad plumes Rooted At The Base Of The Earth's Mantle Beneath Major Hotspots, *Nature*, **525**, 95–99.

Fuchs, K. & Müller, G., 1971. Computation of synthetic seismograms with the reflectivity method and comparison with observations, *Geophys. J. R. astr. Soc.*, **23**, 417–433.

Furumura, T., Kennett, B. L. N. & Takenaka, H., 1998a. Parallel 3-D pseudospectral simulation of wave propagation, *Geophysics*, **63**, 279–288.

Furumura, M., Kennett, B. L. N. & Furumura, T., 1998b. Anomalous surface waves associated with deep earthquakes, generated at an ocean ridge, *Geophys. J. Int.*, **135**, 845–860.

Furumura, T. & Kennett, B. L. N., 2008. A scattering waveguide in the heterogeneous subducting plate, in *Scattering of Short-Period Seismic Waves*

in Earth Heterogeneity, pp. 195–217, eds. Sato, H. & Fehler, M., Advances in Geophysics, Elsevier.

Fuji, N., Kawai, K. & Geller, R. J., 2010. A methodology for inversion of broad-band seismic waveforms for elastic and anelastic structure and its application to the mantle transition zone beneath the northwestern Pacific, *Phys. Earth Planet. Inter.*, **180**, 118–137.

Geller, R. J. & Hara, T., 1993. Two efficient algorithms for iterative linearized inversion of seismic waveform data, *Geophys. J. Int.*, **115**, 699–710.

Geller, R. J. & Ohminato, T., 1994. Computation of synthetic seismograms and their partial derivatives for heterogeneous media with arbitrary natural boundary conditions using the Direct Solution Method, *Geophys. J. Int.*, **116**, 421–446.

Geller, R. J. & Takeuchi, N., 1995. A new method for computing highly accurate DSM synthetic seismograms, *Geophys. J. Int.*, **123**, 449–470.

Geller, R. J. & Takeuchi, N., 1998. Optimally accurate second order time domain finite difference scheme for the elastic equation of motion, *Geophys. J. Int.*, **135**, 48–62.

Geller, R. J., Mizutani, H. & Hirabayashi, N., 2012. Existence of a second island of stability of predictor–corrector schemes for calculating synthetic seismograms, *Geophys. J. Int.*, **188**, 253–262.

Geller, R. J., Mizutani, H., Hirabayashi, N. & Takeuchi, N., 2013a. Method for synthesizing numerical operators, system for synthesizing operators, and simulation device, U.S. Patent 8423332.

Geller, R. J., Mizutani, H., Hirabayashi, N. & Takeuchi, N., 2013b. Method for synthesizing numerical operators, system for synthesizing operators, and simulation device: Japan Patent 5,279,016

Gilbert, F., 1970. Excitation of the Normal Modes of the Earth by Earthquake Sources, *Geophys. J. R. astr. Soc.*, **22**, 223–226.

Grand, S. P. & Helmberger, D. V., 1984. Upper mantle shear structure beneath the Northwest Atlantic ocean. *J. Geophys. Res.*, **89**, 1465–1475.

Guo, Y., Koketsu, K. & Ohno, T., 2013. Analysis of the rupture process of the 1995 Kobe earthquake using a 3D velocity structure, *Earth Planets Space*, **65**, 1581–1586.

Hasegawa, K., Geller, R. J. & Hirabayashi, N., 2016. An error analysis of higher-order finite-element methods: effect of degenerate coupling on simulation of elastic wave propagation, *Geophys. J. Int.*, **205**, 1532–1547.

Hori M., Ichimura, T. & Fujita, K., 2016. Simulation of SeismicWave Propagation and Amplification, in *High-Performance Computing for Structural Mechanics and Earthquake/Tsunami Engineering*, eds. Yoshimura, S., Hori, M. & Ohsaki, M., Springer Tracts of Mechanical Engineering.

Igel, H., Mora, P. & Riollet, B., 1995. Anisotropic wave propagation through finite-difference grids, *Geophysics*, **60**, 1203–1216.

Igel, H. & Weber, M., 1995. SH wave propagation in the whole mantle using high-order finite differences, *Geophys. Res. Lett.*, **22**, 731–734.

Igel, H. & Weber, M., 1996. P-SV wave propagation in the Earth's mantle using finite-differences: application to heterogeneous lowermost mantle structure, *Geophys. Res. Lett.*, **23**, 415–418.

Igel, H., 1999. Wave propagation in three-dimensional spherical sections by the Chebyshev spectral method, *Geophys. J. Int.*, **136**, 559–566.

Igel, H., Nissen-Meyer, T. & Jahnke, G., 2002. Wave propagation in 3-D spherical sections: effects of subduction zones, *Phys. Earth planet. Inter.*, **132**, 219–234.

Igel, H., 2016. *Computational Seismology: A practical Introduction*, 1st edn., Oxford University Press, New York.

Ishii, M. & Tromp, J., 1999. Normal-Mode and Free-Air Gravity Constraints on Lateral Variations in Velocity and Density of Earth's Mantle, *Science*, **285**, 1231–1236.

Jahnke, G., Thorne, M. S., Cochard, A. & Igel, H., 2008. Global SH-wave propagation using a parallel axisymmetric spherical finite-difference scheme: application to whole mantle scattering, *Geophys. J. Int.*, **173**, 815–826.

Karniadakis, G. & Sherwin, S., 2005. *Spectral/hp Element Methods for Computational Fluid Dynamics*, 2nd edn., Oxford University Press, New York.

Käser, M. & Dumbser. M., 2006. An arbitrary high order discontinuous Galerkin method for elastic waves on unstructured meshes II: The three-dimensional isotropic case, *Geophys. J. Int.*, **167**, 319–336.

Kawai, K., Takeuchi, N. & Geller, R. J., 2006. Complete synthetic seismograms up to 2 Hz for transversely isotropic spherically symmetric media, *Geophys. J. Int.*, **164**, 411–424.

Kawai, K., Geller, R. J. & Fuji, N., 2007a. D″ beneath the Arctic from inversion of shear waveforms. *Geophys. Res. Lett.*, **34**, L21305.

Kawai, K., Takeuchi, N., Geller, R. J. & Fuji, N., 2007b. Possible evidence for a double crossing phase transition in D″ beneath Central America from inversion of seismic waveforms, *Geophys. Res. Lett.*, **34**, L09314.

Kawai, K., Sekine, S., Fuji, N. & R.J. Geller, R. J., 2009. Waveform inversion for D″ structure beneath northern Asia using Hi-net tiltmeter data, *Geophys. Res. Lett.*, **36**, L20314.

Kawai, K., & Tsuchiya, T., 2009. Temperature profile in the lowermost mantle from seismological and mineral physics joint modeling, *Proc. Natl. Acad. Sci. U.S.A.*, **106**, 22119–22123.

Kawai, K. & Geller, R. J., 2010a. Inversion of seismic waveforms for shear wave velocity structure in the lowermost mantle beneath the Hawaiian hotspot, *Phys. Earth Planet. Inter.*, **183**, 136–142.

Kawai, K., & Geller, R. J., 2010b. The vertical flow in the lowermost mantle beneath the Pacific from inversion of seismic waveforms for anisotropic structure, *Earth Planet. Sci. Lett.*, **297**, 190–198.

Kawai, K. & Geller, R. J., 2010c. Waveform inversion for localized seismic structure and an application to D″ structure beneath the Pacific, *J. Geophys. Res.*, **115**, B01305.

Kawai, K., Geller R. J., & Fuji, N., 2010. Waveform inversion for S-wave structure in the lowermost mantle beneath the Arctic: Implications for mineralogy and chemical composition, *Geophys. Res. Lett.*, **37**, L16301.

Kawai, K., Konishi, K., Geller, R. J. & Fuji, N., 2014. Methods for inversion of body-wave waveforms for localized three-dimensional seismic structure and an application to D″ structure beneath Central America, *Geophys. J. Int.*, **197**, 495–524.

Kay, I. & Krebes, E.S., 1999. Applying finite element analysis to the memory variable formulation of wave propagation in anelastic media, *Geophysics*, **64**, 300–307.

Kelly, K. R., Ward, R. W., Treitel, S. & Alford, R. M., 1976. Synthetic seismograms: a Finite difference approach, *Geophysics*, **41**, 2–27.

Kennett, B.L.N., 1983. *Seismic Wave Propagation in Stratified Media*, Cambridge University Press, Cambridge, UK.

Koketsu, K., 1987. 2-D reflectivity method and synthetic seismograms for irregularly layered structures–I. SH-wave generation, *Geophys. J. R. astr. Soc.*, **89**, 821–838.

Koketsu, K., Kennett, B.L.N. & Takenaka, H., 1991. 2-D reflectivity method and synthetic seismograms for irregularly layered structures–II. Invariant embedding approach, *Geophys. J. Int.*, **105**, 119–130.

Koketsu, K., Fujiwara, H. & Ikegami, Y., 2004. Finite-element simulation of seismic ground motion with a voxel mesh, *Pure Appl. Geophys.*, **161**, 2183–2198.

Kolman, R., Plešek, J., Okrouhlík, M. & Gabriel, D., 2013. Grid dispersion analysis of plane square biquadratic serendipity finite elements in transient elastodynamics, *Int. J. numer. Meth. Engrng.*, **96**, 1–28.

Komatitsch, D., & Vilotte, J. P., 1998. The Spectral Element method: an efficient tool to simulate the seismic response of 2D and 3D geological structures, *Bull. seism. Soc. Am.*, **88**, 368–392

Komatitsch, D. & Tromp, J., 1999. Introduction to the spectral-element method for 3-D seismic wave propagation, *Geophys. J. Int.*, **139**, 806–822.

Komatitsch, D., Barnes, C. & Tromp, J., 2000a. Wave propagation near a fluid-solid interface: a spectral element approach, *Geophysics*, **65**, 623–631.

Komatitsch, D., Barnes, C. & Tromp, J., 2000b. Simulation of anisotropic wave propagation based upon a spectral element method, *Geophysics*, **65**, 1251–1260.

Komatitsch, D. & Tromp, J., 2002a. Spectral-element simulations of global seismic wave propagation, Part I: Validation, *Geophys. J. Int.*, **149**, 390–412.

Komatitsch, D. & Tromp, J., 2002b. Spectral-element simulations of global seismic wave propagation, Part II: 3-D models, oceans, rotation, and gravity, *Geophys. J. Int.*, **150**, 303–318.

Komatitsch, D. & Tromp, J., 2003. A perfectly matched layer absorbing boundary condition for the second-order seismic wave equation, *Geophys. J. Int.*, **154**, 146–153.

Komatitsch, D., Erlebacher, G., Göddeke, D. & Michéa, D., 2010. High-order finite-element seismic wave propagation modeling with MPI on a large GPU cluster, *J. Comput. Phys.*, **229**, 7692–7714.

Konishi, K., Kawai, K., Geller, R. J. & Fuji, N., 2009. MORB in the lowermost mantle beneath the western Pacific: Evidence from waveform inversion, *Earth Planet. Sci. Lett.*, **278**, 219–225.

Konishi, K., Kawai, K., Geller, R. J. & Fuji, N., 2012. Waveform inversion of broad-band body-wave data for the S-velocity structure in the lowermost mantle beneath the Indian subcontinent and Tibetan Plateau, *Geophys. J. Int.*, **191**, 305–316.

Konishi, K., Kawai, K., Geller, R. J. & Fuji, N., 2014. Waveform inversion for localized 3-D seismic velocity structure in the lowermost mantle beneath the Western Pacific, *Geophys. J. Int.*, **199**,1245–1267.

Korn, M., 1987. Computation of wavefields in vertically inhomogeneous media by a frequency domain finite-difference method and application to wave propagation in earth models with random velocity and density perturbations, *Geophys. J. R. astr. Soc.*, **88**, 345–377.

Lax, P. D. & Wendroff, B., 1964. Difference schemes for hyperbolic equations with high order of accuracy, *Commun. Pure appl. Math.*, **17**, 381–398.

Lay, T. & Helmberger, D. V., 1983. A lower mantle S-wave triplication and the shear velocity structure of D″. *Geophys. J. R. Astr. Soc.* **75**, 799–837.

Levander, A.R., 1988. 4th-order finite-difference p-sv seismograms, *Geophysics*, **53**, 1425–1436

Marfurt, K. J., 1984. Accuracy of finite-difference and finite-element modeling of the scalar and elastic wave equation, *Geophysics*, **49**, 533–549.

Moczo, P., Kristek, J., Galis, M., Chaljub, E. & Etienne, V., 2011. 3-D finite-difference, finite-element, discontinuous-Galerkin and spectral-element schemes analysed for their accuracy with respect to P-wave to S-wave speed ratio, *Geophys. J. Int.*, **187**, 1645–1667.

Monteiller, V., Chevrot, S., Komatitsch, D. & Fuji, N., 2013. A hybrid method to compute short period synthetic seismograms of teleseismic body waves in a 3-D regional model, *Geophys. J. Int.*, **192**, 230–247.

Mizutani, H., Geller, R. J. & Takeuchi, N., 2000. Comparison of accuracy and efficiency of time-domain schemes for calculating synthetic seismograms, *Phys. Earth Planet. Int.*, **119**, 75–97.

Mulder, W.A., 1999. Spurious modes in finite-element discretizations of the wave equation may not be all that bad, *Appl. numer. Math.*, **30**, 425–445.

Mullen, R. & Belytschko, T., 1982. Dispersion analysis of finite element semidiscretizations of the two-dimensional wave equation, *Int. J. Numer. Methods Eng.*, **18**, 11–29.

Namiki, A., Sueyoshi, K. & Takeuchi, N., 2013. Can a sheet-like low-velocity region form an elongated Large Igneous Province?, *Geochem. Geophys. Geosys.*, **14**, 3053–3066.

von Neumann, J. & Richtmyer, R. D., 1950. A method for the numerical calculation of hydrodynamic shocks, *J. appl. Phys.*, **21**, 232–237.

Ohminato, T. & Chouet, B. A., 1997. A free-surface boundary condition for including 3D topography in the finite difference method, *Bull. Seism. Soc. Am.*, **87**, 494–515.

Ohminato, T., Takeo, M., Kumagai, H., Yamashina, T., Oikawa, J., Koyama, E., Tsuji, H. & Urabe, T., 2006. Vulcanian eruptions with dominant single

force components observed during the Asama 2004 volcanic activity in Japan, *Earth Planets Space,* **58**, 583–593.

Oliveira, S.P. & Seriani, G., 2011. Effect of element distortion on the numerical dispersion of spectral element methods, *Commun. Comput. Phys.*, **9**, 937–958.

Patera, A.T., 1984. A spectral element method for fluid dynamics: Laminar flow in a channel expansion, *J. Comput. Phys.*, **54**, 468–488.

Ronchi, C., Ianoco, R. & Paolucci, P. S., 1996. The "Cubed Sphere": a new method for the solution of partial differential equations in spherical geometry, *J. Comput. Phys.*, **124**, 93–114.

Seriani, G. & Priolo, E., 1994. Spectral element method for acoustic wave simulation in heterogeneous media, *Finite Elements in Analysis and Design*, **16**, 337–348.

Seriani, G. & Oliveira, S. P., 2008a. Dispersion analysis of spectral element methods for elastic wave propagation, *Wave Motion*, **45**, 729–744.

Seriani, G. & Oliveira, S. P., 2008b. DFT modal analysis of spectral element methods for acoustic wave propagation, *J. Comput. Acoust.*, **16**, 531–561.

Strang, G. & Fix, G. J., 1973. *An Analysis of the Finite Element Method*, Prentice Hall Englewood Cliffs.

Suzuki, Y., Kawai, K., Geller, R. J., Borgeaud, A. F. E. & Konishi, K., 2016. Waveform inversion for 3-D S-velocity structure of D″ beneath the Northern

Pacific: possible evidence for a remnant slab and a passive plume, *Earth, Planets and Space*, DOI: 10.1186/s40623-016-0576-0.

Takeuchi, H. & Saito, M., 1972. Seismic surface waves, *Meth. cornput. Phys.*, **11**, 217–295.

Takeuchi, N., Geller, R. J. & Cummins, P. R., 1996. Highly accurate P-SV complete synthetic seismograms using modified DSM operators, *Geophys. Res. Lett.*, **23**, 1175–1178.

Takeuchi, N. & Geller, R. J., 2000. Optimally accurate second order time-domain finite difference scheme for computing synthetic seismograms in 2-D and 3-D media, *Phys. Earth planet. Inter.*, **119**, 99–131.

Takeuchi, N., Geller, R. J. & Cummins, P. R., 2000. Complete synthetic seismograms for 3-D heterogeneous Earth models computed using modified DSM operators and their applicability to inversion for Earth structure, *Phys. Earth Planet. Int.*, **119**, 25–36.

Takeuchi, N. & Geller, R. J., 2003. Accurate Numerical Methods for Solving the Elastic Equation of Motion for Arbitrary Source Locations, *Geophys. J. Int.*, **154**, 852–866.

Takeuchi, N., 2007. Whole mantle SH-velocity model constrained by waveform inversion based on three-dimensional Born kernels, *Geophys. J. Int.*, **169**, 1153–1163.

Thompson, L.L. & Pinsky, P.M., 1994. Complex wavenumber Fourier analysis of the p-version finite element method, *Comput. Mech.*, **13**, 255–275.

To, A., Romanowicz, B., Capdeville, Y. & Takeuchi, N., 2005. 3D effects of sharp boundaries at the borders of the African and Pacific Superplumes: Observation and modeling, *Earth Planet. Sci. Lett.*, **233**, 137–153.

To, A., Fukao, Y. & Tsuboi, S., 2011. Evidence for a thick and localized ultra low shear velocity zone at the base of the mantle beneath the central Pacific, *Phys. Earth planet. Inter.*, **184**, 119–133.

Virieux, J., 1984, SH wave propagation in heterogeneous media: velocity-stress finite-difference method, *Geophysics*, **49**, 1933–1957.

Virieux, J., 1986, P-SV wave propagation in heterogeneous media: velocity-stress finite-difference method, *Geophysics*, **51**, 889–901.

Wen, L. X. & Helmberger, D. V., 1998. A two-dimensional P-SV hybrid method and its application to modeling localized structures near the core-mantle boundary, *J. Geophys. Res.*, **103**, 17,901–17,918.

Woodhouse, J. H., 1988. The calculation of eigenfrequencies and eigenfunctions of the free oscillations of the Earth and the Sun, in *Seismological Algorithms, Computational Methods and Computer Programs*, pp. 321–370, ed. Doornbos, D. J., Academic Press, London.

Wu, R. S. & Zheng, Y., 2014. Non-linear partial derivative and its De Wolf approximation for non-linear seismic inversion, *Geophys. J. Int.*, **196**, 1827–1843.

Zahradník, J. & Moczo, P., 1996. Hybrid seismic modeling based on discrete-wave number and finite-difference methods, *Pure Appl. Geophys.*, **148**, 21–38

Zhang, J. & Verschuur, D. J., 2002. Elastic wave propagation in heterogeneous anisotropic media using the lumped finite-element method, *Geophysics*, **67**, 625–638.

Zhang, W., Shen, Y. & Zhao, L., 2012. Three-dimensional anisotropic seismic wave modelling in spherical coordinates by a collocated-grid finite-difference method, *Geophys. J. Int.*, **188**, 1359–1381.

Appendix A

Error analysis of SEM I: effect of degenerate coupling

Waveform inversion for Earth structure (e.g., Fichtner *et al.* 2013; Kawai *et al.* 2014) requires accurate methods for computing synthetic seismograms. Many higher order finite-element methods have been proposed for use in computing synthetic seismograms, notably SEM (e.g., Komatitsch & Vilotte 1998). Most error analyses of ho-FEMs including SEM have emphasized dispersion analysis (e.g., De Basabe & Sen 2007; Seriani & Oliveira 2008ab; Ainsworth & Wajid 2009; Kolman *et al.* 2013), but Thompson & Pinsky (1994) and Mulder (1999) also studied the errors of eigenfunctions for a 1-D case. Moczo *et al.* (2011) conducted an analysis of the "local error" of many numerical schemes, including ho-FEMs, and studied its dependence on the P-wave to S-wave velocity ratio on the basis of both theory and numerical experiments.

The purpose of this appendix is to derive a theoretical framework for making a

systematic study of the error of synthetic seismograms computed using ho-FEMs, rather than just the dispersion error. We show the existence of a previously unrecognized type of error due to degenerate coupling between waves with the same frequency but different wavenumbers. We confirm this result by conducting numerical experiments for an application of SEM to the 2-D elastic case using methods similar to those used by Mulder (1999) for the 1-D case.

A significant portion of this appendix was published in *Geophysical Journal International* (2016, vol. 205, 1532–1547).

To avoid confusion, in the following appendices we use the word "cell" as volume element of FEM, and use the word "element" as the elements of matrices.

A.1 Theory for formal estimates of numerical error

We begin by reviewing GT95 derivation of the theory for making formal estimates of the error of numerical solutions of the elastic equation of motion, which we then extend to the case of modes with equal or nearly equal frequencies. The derivation of GT95 is for a frequency-domain scheme. The extension to time-domain schemes is given by GT98 and TG00 and to predictor-corrector time domain schemes by GMH12.

GT95 represent all numerical schemes in the framework of the weak form of the elastic equation of motion (e.g., Geller & Ohminato 1994). The discretized equation of motion for a heterogeneous elastic medium with free surface boundary conditions

is given by

$$\left(\omega^2\mathbf{T}-\mathbf{H}\right)\mathbf{c}=-\mathbf{g}, \tag{A.1}$$

where ω is the frequency, $\mathbf{T}$ is the mass matrix, $\mathbf{H}$ is the stiffness matrix, $\mathbf{c}$ is the vector of expansion coefficients for the trial functions, and $\mathbf{g}$ is the discretized force vector. In the basis of trial functions, the elements of the mass matrix, the stiffness matrix, and the force vector are given respectively by

$$[\mathbf{T}]_{ij}=\int_V\left[\phi_\alpha^{(i)}\right]^*\rho\phi_\alpha^{(j)}dV \tag{A.2}$$

$$[\mathbf{H}]_{ij}=\int_V\left[\phi_{\alpha,\beta}^{(i)}\right]^*C_{\alpha\beta\mu\nu}\phi_{\mu,\nu}^{(j)}dV \tag{A.3}$$

$$[\mathbf{g}]_i=\int_V\left[\phi_\alpha^{(i)}\right]^*f_\alpha dV, \tag{A.4}$$

where "$[\cdot]_{ij}$" and "$[\cdot]_i$" represent the elements in the basis of trial functions, α, β, μ, and ν represent dummy indices for the x, y or z axes, and summation over repeated subscript indices is implied. $\phi_\alpha^{(i)}$ is the α-component of the ith trial function, "$_{,\beta}$" denotes spatial differentiation with respect to the β-coordinate, ρ is the density, $C_{\alpha\beta\mu\nu}$ is the elastic modulus, f_α is the external body force, and V denotes the entire volume of the medium. The displacement is represented as a linear combination of the trial functions:

$$u_\alpha=\sum_i[\mathbf{c}]_i\phi_\alpha^{(i)}. \tag{A.5}$$

We formally denote the exact operators by $\mathbf{T}^{(0)}$ and $\mathbf{H}^{(0)}$, the exact solution by $\mathbf{c}^{(0)}$, the numerical operators by $\mathbf{T}$ and $\mathbf{H}$, the error of the numerical operators by

$\boldsymbol{\delta}\mathbf{T}$ and $\boldsymbol{\delta}\mathbf{H}$, and the error of the numerical solution by $\boldsymbol{\delta}\mathbf{c}$, where

$$\mathbf{T} = \mathbf{T}^{(0)} + \boldsymbol{\delta}\mathbf{T} \tag{A.6}$$

$$\mathbf{H} = \mathbf{H}^{(0)} + \boldsymbol{\delta}\mathbf{H} \tag{A.7}$$

$$\mathbf{c} = \mathbf{c}^{(0)} + \boldsymbol{\delta}\mathbf{c}. \tag{A.8}$$

The eigenvalue problem for the exact operators is

$$\left[\omega_i^2\mathbf{T}^{(0)} - \mathbf{H}^{(0)}\right]\mathbf{c}_i = 0, \tag{A.9}$$

where ω_i is the eigenfrequency of the ith mode, and $\mathbf{c}_i$ is the eigenvector. The modes are orthonormalized as follows:

$$\mathbf{c}_i^*\mathbf{H}^{(0)}\mathbf{c}_j = \omega_i^2\mathbf{c}_i^*\mathbf{T}^{(0)}\mathbf{c}_j = \omega_i^2\delta_{ij}, \tag{A.10}$$

where the superscript * indicates the conjugate transpose, and δ_{ij} is a Kronecker-δ.

The exact equation of motion can be formally written as follows:

$$\left[\omega^2\mathbf{T}^{(0)} - \mathbf{H}^{(0)}\right]\mathbf{c}^{(0)} = -\mathbf{g}. \tag{A.11}$$

The error of the solutions, $\boldsymbol{\delta}\mathbf{c}$, can be estimated using the first-order Born approximation:

$$\left[\omega^2\mathbf{T}^{(0)} - \mathbf{H}^{(0)}\right]\boldsymbol{\delta}\mathbf{c} = -\left(\omega^2\boldsymbol{\delta}\mathbf{T} - \boldsymbol{\delta}\mathbf{H}\right)\mathbf{c}^{(0)}. \tag{A.12}$$

We represent the solution of eq. (A.11) in terms of an eigenfunction expansion,

$$\mathbf{c}^{(0)} = \sum_i d_i^{(0)} \mathbf{c}_i. \tag{A.13}$$

The expansion coefficient of the ith mode is given by

$$d_i^{(0)} = -g_i / \left(\omega^2 - \omega_i^2\right), \tag{A.14}$$

where

$$g_i = \mathbf{c}_i^* \mathbf{g}. \tag{A.15}$$

The denominator of the right-hand side of eq. (A.14) will be small, and thus $d_i^{(0)}$ will be large, when ω is close to ω_i. $d_i^{(0)}$ will be negligible except when ω is in the vicinity of ω_i.

GT95 did not discuss the case in which several modes have identical or nearly identical eigenfrequencies; we consider that case below, but for the moment we continue with the derivation of GT95. We also represent the solution of eq. (A.12) in terms of an eigenfunction expansion,

$$\boldsymbol{\delta}\mathbf{c} = \sum_i \delta d_i \mathbf{c}_i. \tag{A.16}$$

The expansion coefficient for the ith mode is given by

$$\delta d_i = -\frac{\sum_j \left(\omega^2 \delta T_{ij} - \delta H_{ij}\right) d_j^{(0)}}{\omega^2 - \omega_i^2}, \tag{A.17}$$

where the matrix elements in eq. (A.17) are given by

$$\delta T_{ij} = \mathbf{c}_i^* \boldsymbol{\delta}\mathbf{T}\mathbf{c}_j, \quad \delta H_{ij} = \mathbf{c}_i^* \boldsymbol{\delta}\mathbf{H}\mathbf{c}_j. \tag{A.18}$$

GT95 considered the case in which there were no other modes with frequencies equal or nearly equal to ω_i. For that case, by the same argument used above for eq. (A.14), the i-component of the error (i.e., δd_i) will be large only when ω is close to ω_i. However, in the vicinity of $\omega = \omega_i$, only $d_i^{(0)}$ will be large; the expansion coefficients of all the other modes will be negligible. Therefore in the vicinity of $\omega = \omega_i$, the $j \neq i$ terms in the summation in eq. (A.17) can be neglected. The expansion coefficient of the ith mode is therefore approximately given by

$$\delta d_i = -\frac{(\omega^2 \delta T_{ii} - \delta H_{ii})\, d_i^{(0)}}{\omega^2 - \omega_i^2}. \tag{A.19}$$

We thus see from eq. (A.19) that the relative error of the numerical solution in the vicinity of $\omega = \omega_i$ can be approximated by

$$\frac{\delta d_i}{d_i^{(0)}} = -\frac{\omega^2 \delta T_{ii} - \delta H_{ii}}{\omega^2 - \omega_i^2} = -\frac{\delta T_{ii}\,(\omega^2 - \delta H_{ii}/\delta T_{ii})}{\omega^2 - \omega_i^2}. \tag{A.20}$$

Eq. (A.20) shows that in general the relative error will greatly increase as $\omega \to \omega_i$. However, if the numerator of eq. (A.20) is also proportional to $(\omega^2 - \omega_i^2)$, the relative error will not worsen appreciably as $\omega \to \omega_i$. Such proportionality can be achieved

if and only if the respective errors of the numerical operators approximately satisfy

$$\omega_i^2 \delta T_{ii} - \delta H_{ii} = 0 \tag{A.21}$$

for every mode. GT95 refer to schemes whose operators approximately satisfy eq. (A.21) as "optimally accurate."

The above results show that under the assumptions made in the above derivation only the diagonal matrix elements significantly affect the error of the numerical solution and that the matrix elements for coupling between modes, δT_{ij} and δH_{ij}, $i \neq j$, do not significantly affect the error of the numerical solution. Eq. (A.20) shows that the relative error of the numerical solution obtained using operators that approximately satisfy eq. (A.21) is approximately given by

$$\left| \frac{\delta d_i}{d_i^{(0)}} \right| = |\delta T_{ii}| \,, \tag{A.22}$$

as $\omega \to \omega_i$. On the other hand, if the operators do not approximately satisfy eq. (A.21), then eq. (A.20) shows that the relative error will worsen drastically as $\omega \to \omega_i$.

The eigenproblem for the numerical operators is

$$\left[\left(\omega_i^{(num)} \right)^2 \mathbf{T} - \mathbf{H} \right] \mathbf{c}_i^{(num)} = 0. \tag{A.23}$$

Omitting details, we note that GT95 (see their eq. 2.28) showed, using first-order perturbation theory, that the error of the eigenfrequencies of the numerical operators

is given by

$$\left(\omega_i^{(num)}\right)^2 - \omega_i^2 \approx 2\omega_i \delta\omega_i \approx \delta H_{ii} - \omega_i^2 \delta T_{ii}. \tag{A.24}$$

Thus eq. (A.21), which GT95 derived by minimizing the error of the numerical solution, can also be derived by requiring the error of the eigenfrequencies of the numerical operators (i.e., the solutions of eq. A.23) to be approximately equal to zero. Since the modes are a complete set, the sum of all the modes yields a complete synthetic seismogram. If the eigenfrequencies are all accurate to some given order, the velocity of P and S-waves in the numerical solutions will be accurate to the same order. Note that the eigenfrequencies for a heterogeneous medium play the same role as the phase velocities for a homogeneous medium. Thus suppressing numerical dispersion is equivalent to minimizing the error of the eigenfrequencies of the numerical solutions.

Now let us return to eq. (A.17), above, in GT95's derivation and consider the case for which two or more modes have identical or nearly identical eigenvalues. For the optimally accurate $O(2,2)$ finite difference operators considered by GT95 and the 2-D and 3-D optimally accurate time-domain schemes of TG00 and GMHT13 we have

$$\boldsymbol{\delta}\mathbf{T} \approx F\mathbf{T}^{(0)}, \quad \boldsymbol{\delta}\mathbf{H} \approx F\mathbf{H}^{(0)}, \tag{A.25}$$

where F is a constant. Thus for $i \neq j$, $\delta T_{ij} \approx 0$ and $\delta H_{ij} \approx 0$, and the GT95 derivation holds approximately even for the case of equal or nearly equal eigenvalues (as coupling between modes can be neglected in eq. A.17 because the relevant matrix elements are nearly zero). On the other hand, if there are modes with nearly

identical or identical frequencies for the more general case where

$$\delta H_{ij} \neq 0, \quad \delta T_{ij} \neq 0 \quad \text{for} \quad i \neq j, \tag{A.26}$$

then we cannot reduce eq. (A.17) to eq. (A.19). For this case we can have large errors in the numerical solution even when the numerical operators are designed so that $\delta\omega_i$ in eq. (A.24) is zero, because the relative solution error $|\delta u/u|$ can greatly increase for degenerate or nearly degenerate cases.

A.1.1 Perturbation theory for degenerate cases: a simple example

We consider a case where the first and second modes of the exact problem have the same eigenfrequency:

$$\omega_{ide} = \omega_1 = \omega_2, \tag{A.27}$$

and all the other modes have different eigenfrequencies. For this case we no longer can use eq. (A.24) to estimate the eigenfrequencies of the numerical operators. We must instead solve the following eigenvalue problem:

$$\begin{pmatrix} \delta H_{11} - \omega_{ide}^2 \delta T_{11} & \delta H_{12} - \omega_{ide}^2 \delta T_{12} \\ \delta H_{21} - \omega_{ide}^2 \delta T_{21} & \delta H_{22} - \omega_{ide}^2 \delta T_{22} \end{pmatrix} \begin{pmatrix} a_{i1} \\ a_{i2} \end{pmatrix} \approx 2\omega_{ide}\delta\omega_i \begin{pmatrix} a_{i1} \\ a_{i2} \end{pmatrix} \quad \text{for} \quad i = 1, 2 \tag{A.28}$$

to obtain the two sets of expansion coefficients $\mathbf{a}_i$ and the estimated values of the two respective eigenfrequencies of the numerical operators $\omega_{ide} + \delta\omega_i$ $(i = 1, 2)$. Even if the exact eigenfrequencies are identical, the numerical eigenfrequencies will

in general be split ($\delta\omega_1 \neq \delta\omega_2$) , and we assume that to be the case here.

We now show in more detail how the splitting causes inaccuracies in the numerical solution. For simplicity, we consider a case where the force vector $\mathbf{g}$ has a non-zero value for the first mode ($g_1 \neq 0$), and all of the other components are zero ($g_i = 0$ for $i \neq 1$). For this case, only the first mode should be excited. However, the expansion coefficient of the numerical solution for the second mode is

$$\frac{\delta d_2}{|\mathbf{d}^{(0)}|} = \frac{\delta d_2}{d_1^{(0)}} = -\delta T_{21} - 2a_{12}a_{22}\omega_{ide}\frac{\delta\omega_1 - \delta\omega_2}{\omega^2 - \omega_{ide}^2}, \tag{A.29}$$

where we normalized the eigenfunctions as follows:

$$|a_{i1}|^2 + |a_{i2}|^2 = 1 \tag{A.30}$$

$$\det\begin{pmatrix} a_{11} & a_{12} \\ a_{21} & a_{22} \end{pmatrix} = 1. \tag{A.31}$$

When ω is close to ω_{ide}, the denominator of the second term in eq. (A.29) will be close to zero. Thus δd_2 will in general be large unless the numerator of the second term of (A.29) is zero (i.e., unless there is no splitting), which will in general not be the case. Thus the splitting will in general cause an artificial excitation of the second mode in the numerical solution, except that if the numerical operators approximately satisfy eq. (A.27), this will not occur because the 2×2 matrix in eq. (A.28) is diagonal and a_{12} is zero, and therefore the second term in eq. (A.29) will be zero. We present a simple example in the next section to show the occurrence of such errors due to degenerate coupling in elastic wave simulations using SEM.

A.2 Numerical experiment

We now consider a simple computational example which shows the effects of degenerate coupling. We proceed as follows. In Section A.2.1, we discretize the weak form of the elastic equation of motion using SEM, and in section A.2.2 we specialize this derivation to the case of a homogeneous medium. In Section A.2.3, we use these results to derive the solution for the initial condition of a plane wave at time $t = 0$. We show that the problem can be reduced to a matrix equation for a single cell, giving an easily solvable problem. In Section A.2.4, we show how to find frequency-wavenumber pairs for which degenerate coupling occurs. In Section A.2.5, we show that the error of the numerical solutions degrades in the vicinity of the degenerate frequency-wavenumber pairs, as predicted by our theoretical results.

A.2.1 SEM discretization

We consider a 2-D infinite homogeneous medium, with x and y as the independent variables. The Galerkin discretized form of the homogeneous equation of motion (i.e., the equation for the case of no applied external force) in the time-domain is given by:

$$\int_V \rho \left[\phi_\alpha^{(m)}\right]^* \ddot{u}_\alpha dV + \int_V \left[\phi_{\alpha,\beta}^{(m)}\right]^* C_{\alpha\beta\mu\nu} u_{\mu,\nu} dV = 0 \quad \text{for each value of } m, \qquad \text{(A.32)}$$

where $\phi_\alpha^{(m)}$ is the α-component of the mth trial function, u_α is the α-component of the displacement, and $\ddot{u}_\alpha$ is the α-component of the acceleration. The displacement

$u_\alpha(t,x,y)$ is expressed in terms of a trial function expansion as follows:

$$u_\alpha(t,x,y) = \sum_n d_n(t)\phi_\alpha^{(n)}(x,y), \tag{A.33}$$

where $d_n(t)$ are the expansion coefficients of the trial functions.

We divide the whole space V into a uniform cartesian mesh with cells whose sides have length h. At this point we are using m as a generic index for the trial functions; the numbering for our particular case is discussed below. We define the coordinates of the nodes of the mesh to be

$$(x_{N_x}, y_{N_y}) = (hN_x, hN_y), \tag{A.34}$$

where N_x and N_y, the indices denoting the cells (and also denoting the node at the lower left corner of each cell), span all integers. Then the domain of integration of eq. (A.32) is divided as follows:

$$\sum_{N_x=-\infty}^{\infty}\sum_{N_y=-\infty}^{\infty}\left\{\int_0^h\int_0^h \rho\left[\phi_\alpha^{(m)}(x+hN_x,y+hN_y)\right]^* \ddot{u}_\alpha(t,x+hN_x,y+hN_y)dxdy \right.$$
$$\left. + \int_0^h\int_0^h \left[\phi_{\alpha,\beta}^{(m)}(x+hN_x,y+hN_y)\right]^* C_{\alpha\beta\mu\nu}u_{\mu,\nu}(t,x+hN_x,y+hN_y)dxdy\right\} = 0. \tag{A.35}$$

Note that, for simplicity, we omit explicit mention of the fact that the equations apply to each value of m in eq. (A.35) and below.

A.2.2 SEM formulation for homogeneous medium

We henceforth restrict our discussion to the case of a homogeneous 2-D medium. Thus in the remainder of this appendix ρ and $C_{\alpha\beta\mu\nu}$ are constants. We now define trial functions for a single cell. Most SEM implementations use Legendre-Lagrange interpolation for shape functions in conjunction with the Gauss-Lobatto-Legendre (GLL) quadrature rule (see, e.g., Karniadakis & Sherwin 2005 for a general discussion). For SEM of polynomial order n, we define GLL points as follows for a single cell $0 \leq x, y \leq h$:

$$x_0 = y_0 = 0 < x_1 = y_1 < \cdots < x_n = y_n = h. \tag{A.36}$$

Note that the values in eq. (A.36) are for the GLL interpolation points within a single cell and should not be confused with the coordinates of the corners of the cells defined in eq. (A.34).

We write the scalar SEM interpolation functions within a single cell, $0 \leq x, y \leq h$, as follows:

$$s^{(p_x,p_y)}(x,y) \quad \text{for} \quad p_x = 0, \cdots, n; p_y = 0, \cdots, n, \tag{A.37}$$

Note that we follow the standard definition of the scalar SEM interpolations functions, so that $s^{(p_x,p_y)}(x,y) = 1$ at the point (x_{p_x}, y_{p_y}) and is equal to 0 at all of the other SEM interpolation points.

We next define vector SEM interpolation functions as follows:

$$s_i^{(q)}(x,y) \ = s^{(p_x,p_y)}(x,y)\delta_{i\eta}, \tag{A.38}$$

where η is the coordinate direction (either x or y) for which the vector SEM interpolation function is non-zero at the point (x_{p_x}, y_{p_y}), and where q is a pointer to (η, p_x, p_y). Each pointer to a vector SEM interpolation function has three indices, but through straightfoward bookkeeping they can be arranged in a one-dimension array for ease of computation (see Appendix A4 of Geller & Ohminato 1994 for one example). There are $(n+1)^2$ scalar SEM interpolation functions and $2(n+1)^2$ vector SEM interpolation functions for a single cell; thus the indices of the vector SEM interpolation functions in eq. (A.38) are in the range $1 \leq q \leq 2(n+1)^2$.

We now consider the (N_x, N_y)-th cell, for which

$$\begin{cases} hN_x \leq x \leq h(N_x+1) \\ hN_y \leq y \leq h(N_y+1), \end{cases} \tag{A.39}$$

and we define trial functions such that continuity of displacement is satisfied at the inter-node boundaries. We write the mth trial function in this cell, $\phi_i^{(m)}(x + hN_x, y + hN_y)$, as a linear combination of the vector SEM interpolation functions:

$$\phi_i^{(m)}(x + hN_x, y + hN_y) = \sum_q \left[\mathbf{\Phi}^{(m;N_x,N_y)} \right]_q s_i^{(q)}(x, y), \tag{A.40}$$

where $\mathbf{\Phi}^{(m;N_x,N_y)}$ are the vectors of the expansion coefficients of the vector interpolation functions of SEM, and where "$[\cdot]_q$" represents the qth element of the vector in the brackets. The coefficients of the trial functions must be chosen so that displacement is continuous at nodes on the cell boundaries.

The α-component of the trial functions at the GLL points are given by:

$$\phi_\alpha^{(m)}(x_{p_x} + hN_x, y_{p_y} + hN_y) = \left[\mathbf{\Phi}^{(m;N_x,N_y)}\right]_q. \tag{A.41}$$

To satisfy continuity of the trial functions at inter-cell boundaries, we require the expansion coefficients to satisfy the following conditions:

$$\left[\mathbf{\Phi}^{(m;N_x+1,N_y)}\right]_{(\alpha,0,p_y)} = \left[\mathbf{\Phi}^{(m;N_x,N_y)}\right]_{(\alpha,n,p_y)} \tag{A.42}$$

$$\left[\mathbf{\Phi}^{(m;N_x,N_y+1)}\right]_{(\alpha,p_x,0)} = \left[\mathbf{\Phi}^{(m;N_x,N_y)}\right]_{(\alpha,p_x,n)}. \tag{A.43}$$

We now express the displacement as a linear combination of the trial functions, as shown in eq. (A.33), and then substitute this expansion into eq. (A.35) to obtain the following system of linear equations:

$$\mathbf{T}^G\ddot{\mathbf{d}}(t) + \mathbf{H}^G\mathbf{d}(t) = 0, \tag{A.44}$$

where $\mathbf{T}^G$ and $\mathbf{H}^G$ are the global mass and stiffness matrices, respectively. The element of the local mass and stiffness matrices, $\mathbf{T}^L$ and $\mathbf{H}^L$, respectively, in a single cell are

$$T_{qr}^L = \int_0^h \int_0^h s_i^{(q)} \rho s_i^{(r)} dxdy \tag{A.45}$$

$$H_{qr}^L = \int_0^h \int_0^h s_{i,j}^{(q)} C_{ijkl} s_{k,l}^{(r)} dxdy, \tag{A.46}$$

where the integrations in eqs. (A.45) and (A.46) are approximately calculated using

GLL quadrature. The local matrices for each cell are overlapped following standard ho-FEMs so that the continuity conditions (eqs. A.42 and A.43) are satisfied when assembling the global matrices in eq. (A.44).

In this appendix, we omit the explicit forms of the interpolation functions and the details of the implementation of the SEM.

A.2.3 Formulation of numerical experiment

The discussion in Section A.2.1 is for a general case and that in Section A.2.2 for the homogeneous case in general. In this section, however, we derive results for a particular simple case. We solve eq. (A.44) for the case of an infinite, homogeneous, isotropic medium where the initial conditions are a harmonic plane wave for the displacement and velocity field at $t = 0$. The discretized form of a harmonic plane wave with wavenumber vector

$$\vec{\mathbf{k}} = (k_x, k_y) \tag{A.47}$$

(Note that we are using the arrow over the wavenumber vector $\vec{\mathbf{k}}$ to indicate a physical vector as opposed to a vector in the sense of linear algebra.) is

$$\begin{aligned}\left[\boldsymbol{\psi}^{(N_x,N_y)}(t;\vec{\mathbf{k}})\right]_q &= A_\alpha \exp\left(\mathrm{i}k_x(x_{p_x} + hN_x) + \mathrm{i}k_y(y_{p_y} + hN_y) - \mathrm{i}\omega t\right) \\ &= A_\alpha \exp\left(\mathrm{i}k_x x_{p_x} + \mathrm{i}k_y y_{p_y} - \mathrm{i}\omega t\right) \exp(\mathrm{i}k_x hN_x + \mathrm{i}k_y hN_y) \\ &= \left[\boldsymbol{\psi}^{(0,0)}(t;\vec{\mathbf{k}})\right]_q \exp(\mathrm{i}k_x hN_x + \mathrm{i}k_y hN_y),\end{aligned} \tag{A.48}$$

where $\mathrm{i} = \sqrt{-1}$, q is, as discussed above, a pointer to one of the vector SEM interpolation functions, and

$$\left[\boldsymbol{\psi}^{(0,0)}(t;\vec{\mathbf{k}})\right]_q = A_\alpha \exp(\mathrm{i}k_x x_{p_x} + \mathrm{i}k_y y_{p_y} - \mathrm{i}\omega t). \tag{A.49}$$

Note that the last line of eq. (A.48) shows that the discretized plane wave for an arbitrary cell can be easily expressed in terms of that for the $(0,0)$-th cell. The amplitude vector is

$$\vec{\mathbf{A}} = (A_x, A_y) = D(k_x, k_y) \tag{A.50}$$

for P-waves and

$$\vec{\mathbf{A}} = (A_x, A_y) = D(-k_y, k_x) \tag{A.51}$$

for S-waves, where without loss of generality

$$D = (k_x^2 + k_y^2)^{-1/2}, \tag{A.52}$$

and ω is the frequency given by

$$\omega = c\sqrt{k_x^2 + k_y^2}, \tag{A.53}$$

where

$$c = \sqrt{(\lambda + 2\mu)/\rho} \tag{A.54}$$

for P-waves and

$$c = \sqrt{\mu/\rho} \tag{A.55}$$

for S-waves, where λ and μ are the Lamé constants and ρ is the density.

We specify the respective initial conditions for the displacement and velocity to be as follows:

$$\mathbf{u}^{(N_x,N_y)}(0) = \boldsymbol{\psi}^{(N_x,N_y)}(0;\vec{\mathbf{k}}) \tag{A.56}$$

$$\dot{\mathbf{u}}^{(N_x,N_y)}(0) = \dot{\boldsymbol{\psi}}^{(N_x,N_y)}(0;\vec{\mathbf{k}}). \tag{A.57}$$

The physically meaningful range of the wavenumbers in eq. (A.48) is

$$-\pi n/h = -k_{\max} < k_x, k_y \leq k_{\max} = \pi n/h, \tag{A.58}$$

where $k_{\max}$ corresponds to the Nyquist sampling rate.

We now show that eq. (A.44) with the initial conditions eqs. (A.56) and (A.57) can be reduced to $2n^2$ simultaneous differential equations, and that the numerical wavefield calculated by SEM can be written in the same form as the last line of eq. (A.48), with $\boldsymbol{\psi}^{(0,0)}(t;\vec{\mathbf{k}})$ replaced by any other function. Such functions are called Bloch functions (e.g., Brillouin 1953).

We assume the following form for $\boldsymbol{\Phi}^{(m;N_x,N_y)}$

$$\boldsymbol{\Phi}^{(m;N_x,N_y)} = \mathbf{z}^{(q)}(\vec{\mathbf{k}}) \exp(\mathrm{i}k_x h N_x + \mathrm{i}k_y h N_y), \tag{A.59}$$

where the index of the trial functions, m, is replaced by q and $\vec{\mathbf{k}}$. The physical meaning of eq. (A.59) is that the global trial functions are defined as Bloch functions, where the vectors $\mathbf{z}^{(q)}(\vec{\mathbf{k}})$ are basis vectors for a single cell, defined as follows.

The global trial functions in eq. (A.59) must satisfy the continuity conditions

eqs. (A.42) and (A.43). We thus require the following relation between the values of the single-cell basis vectors at bottom and top boundaries, and the left and right boundaries, respectively:

$$\left[\mathbf{z}^{(q)}(\vec{\mathbf{k}})\right]_{(\alpha,0,p_y)} = \left[\mathbf{z}^{(q)}(\vec{\mathbf{k}})\right]_{(\alpha,n,p_y)} \exp(-\mathrm{i}k_x h) \tag{A.60}$$

$$\left[\mathbf{z}^{(q)}(\vec{\mathbf{k}})\right]_{(\alpha,p_x,0)} = \left[\mathbf{z}^{(q)}(\vec{\mathbf{k}})\right]_{(\alpha,p_x,n)} \exp(-\mathrm{i}k_y h). \tag{A.61}$$

As an example, Fig. A.1 shows the GLL nodes of a cell for $n = 4$. The circles indicate linearly independent nodes, and the crosses indicate linearly dependent nodes (due to the boundary conditions in eqs. A.60 and A.61). Note that the choice of which boundary node (right or left; top or bottom; one of the four corners) is linearly independent is arbitrary, but must be the same for every cell in the medium.

For SEM of order n each basis vector $\mathbf{z}^{(q)}(\vec{\mathbf{k}})$ has $2(n+1)^2$ elements which define the x- and y-components of the displacement at each of the SEM interpolation points, but because of the continuity conditions eqs. (A.60) and (A.61) only $2n^2$ basis vectors (each with $2(n+1)^2$ elements) are required. We have three types of basis vectors: $2(n-1)^2$ for interior points, $4(n-1)$ for boundary points other than corners, and 2 for corners, for a total of $2n^2$ basis vectors. We define all of the n^2 basis vectors for the x-component displacements to have the y-component displacement set to zero at all nodes. The basis vectors for internal nodes (see Fig. A.1) are defined to have a value of 1 at one of the internal nodes and zero at all the other nodes. The basis vector for a node on the left hand edge (other than a corner node) is defined to have a displacement of 1 at the left hand edge, and

$\exp(\mathrm{i}k_x h)$ at the corresponding point (the point with the same height) on the right-hand edge, with zeros at all the other nodes. The basis vectors for nodes (other than corner nodes) on the top and bottom edges are defined similarly. Finally, for the case of the basis vector for the corner nodes the element for the lower left hand corner is 1, that for the lower right corner is $\exp(\mathrm{i}k_x h)$, that for the upper left corner is $\exp(\mathrm{i}k_y h)$, and that for the upper right corner is $\exp(\mathrm{i}k_x h)\exp(\mathrm{i}k_y h)$, with the elements for all of the other nodes equal to zero. The basis vectors for the y-component displacements are defined similarly.

The matrix of the $2n^2$ basis vectors for a single cell, each of which has $2(n+1)^2$ elements, is defined as follows:

$$\mathbf{Z}(\vec{\mathbf{k}}) = \left(\mathbf{z}^{(1)}(\vec{\mathbf{k}}), \ldots, \mathbf{z}^{(2n^2)}(\vec{\mathbf{k}})\right), \tag{A.62}$$

where the superscript indices in the above equation refer to the pointers q, which have been arranged in some particular order. We also define a second matrix of $2n^2$ basis vectors for a single cell for $\vec{\mathbf{k}}'$ rather than $\vec{\mathbf{k}}$:

$$\mathbf{Z}(\vec{\mathbf{k}}') = \left(\mathbf{z}^{(1)}(\vec{\mathbf{k}}'), \ldots, \mathbf{z}^{(2n^2)}(\vec{\mathbf{k}}')\right), \tag{A.63}$$

and a second set of trial functions using $\vec{\mathbf{k}}'$ instead of $\vec{\mathbf{k}}$, and $\mathbf{Z}(\vec{\mathbf{k}}')$ rather than $\mathbf{Z}(\vec{\mathbf{k}})$:

$$\mathbf{\Phi}^{(m';N_x,N_y)} = \mathbf{z}^{(q)}(\vec{\mathbf{k}}')\exp(\mathrm{i}k'_x hN_x + \mathrm{i}k'_y hN_y). \tag{A.64}$$

We now use the trial functions in eq. (A.59) in place of those defined in eq. (A.40).

In place of eq. (A.33) the trial function expansion becomes

$$\begin{aligned}\mathbf{d}^{(N_x,N_y)}(t) &= \sum_{\vec{\mathbf{k}}} \sum_{q=1}^{2n^2} \left[\mathbf{v}(t;\vec{\mathbf{k}})\right]_q \mathbf{z}^{(q)}(\vec{\mathbf{k}}) \exp(\mathrm{i}k_x h N_x + \mathrm{i}k_y h N_y) \\ &= \sum_{\vec{\mathbf{k}}} \mathbf{Z}(\vec{\mathrm{k}})\mathbf{v}(t;\vec{\mathbf{k}}) \exp(\mathrm{i}k_x h N_x + \mathrm{i}k_y h N_y), \end{aligned} \tag{A.65}$$

where the sum is taken over all wavenumbers $\vec{\mathbf{k}}$, the range of applicability of eq. (A.65) is the area of the (N_x, N_y)-th element, namely that given by eq. (A.39) and where $\mathbf{v}(t;\vec{\mathbf{k}})$ is a vector of the $2n^2$ unknown coefficients of the single-cell basis vectors.

We now rewrite the equation of motion (eq. A.32 or A.44) using eq. (A.65) to represent the displacement and eq. (A.64) as the trial function by whose complex conjugate we multiply the equation of motion on the left. However, before proceeding we make one simplification to eq. (A.65), dropping the sum over all wavenumbers and considering only a single wavenumber $\vec{\mathbf{k}}$. Eq. (A.65) thus simplifies to the following:

$$\begin{aligned}\mathbf{d}^{(N_x,N_y)}(t) &= \sum_{q=1}^{2n^2} \left[\mathbf{v}(t;\vec{\mathbf{k}})\right]_q \mathbf{z}^{(q)}(\vec{\mathbf{k}}) \exp(\mathrm{i}k_x h N_x + \mathrm{i}k_y h N_y) \\ &= \mathbf{Z}(\vec{\mathrm{k}})\mathbf{v}(t;\vec{\mathbf{k}}) \exp(\mathrm{i}k_x h N_x + \mathrm{i}k_y h N_y). \end{aligned} \tag{A.66}$$

We substitute eq. (A.66) into eq. (A.44). Using the above trial functions and ansatz,

eq. (A.44) becomes

$$
\begin{aligned}
&\sum_{N_x=-\infty}^{\infty}\sum_{N_y=-\infty}^{\infty}\left[\mathbf{\Phi}^{(m';N_x,N_y)}\right]^*\left[\mathbf{T}^L\ddot{\mathbf{d}}^{(N_x,N_y)}(t)+\mathbf{H}^L\mathbf{d}(t)\right]\\
&=\sum_{N_x=-\infty}^{\infty}\sum_{N_y=-\infty}^{\infty}\left[\mathbf{Z}(\vec{\mathbf{k}}')\exp(\mathrm{i}k'_xhN_x+\mathrm{i}k'_yhN_y)\right]^*\\
&\times\left[\mathbf{T}^L\mathbf{Z}(\vec{\mathbf{k}})\ddot{\mathbf{v}}(t;\vec{\mathbf{k}})\exp(\mathrm{i}k_xhN_x+\mathrm{i}k_yhN_y)+\mathbf{H}^L\mathbf{Z}(\vec{\mathbf{k}})\mathbf{v}(t;\vec{\mathbf{k}})\exp(\mathrm{i}k_xhN_x+\mathrm{i}k_yhN_y)\right]\\
&=\left[\mathbf{Z}(\vec{\mathbf{k}}')\right]^*\left[\mathbf{T}^L\mathbf{Z}(\vec{\mathbf{k}})\ddot{\mathbf{v}}(t;\vec{\mathbf{k}})+\mathbf{H}^L\mathbf{Z}(\vec{\mathbf{k}})\mathbf{v}(t;\vec{\mathbf{k}})\right]\\
&\times\sum_{N_x=-\infty}^{\infty}\exp\left[\mathrm{i}(k_x-k'_x)hN_x\right]\sum_{N_y=-\infty}^{\infty}\exp\left[\mathrm{i}(k_y-k'_y)hN_y\right]\\
&=\left[\mathbf{Z}(\vec{\mathbf{k}}')\right]^*\left[\mathbf{T}^L\mathbf{Z}(\vec{\mathbf{k}})\ddot{\mathbf{v}}(t;\vec{\mathbf{k}})+\mathbf{H}^L\mathbf{Z}(\vec{\mathbf{k}})\mathbf{v}(t;\vec{\mathbf{k}})\right]\\
&\times\frac{(2\pi)^2}{h^2}\delta\left(k'_x-k_x-\frac{2\pi M_x}{h}\right)\delta\left(k'_y-k_y-\frac{2\pi M_y}{h}\right)\\
&=0,
\end{aligned}
\tag{A.67}
$$

where M_x and M_y are integers. Therefore the left hand side of eq. (A.67) will be zero unless

$$
\begin{cases}
k'_x=k_x+2\pi M_x/h\\
k'_y=k_y+2\pi M_y/h.
\end{cases}
\tag{A.68}
$$

For all cases for which eq. (A.68) is satisfied, we obtain the following $2n^2$ simultaneous differential equations,

$$
\widetilde{\mathbf{T}}(\vec{\mathbf{k}})\ddot{\mathbf{v}}(t;\vec{\mathbf{k}})+\widetilde{\mathbf{H}}(\vec{\mathbf{k}})\mathbf{v}(t;\vec{\mathbf{k}})=0,
\tag{A.69}
$$

where

$$
\widetilde{\mathbf{T}}(\vec{\mathbf{k}})=\left[\mathbf{Z}(\vec{\mathbf{k}})\right]^*\mathbf{T}^L\mathbf{Z}(\vec{\mathbf{k}})
\tag{A.70}
$$

$$\widetilde{\mathbf{H}}(\vec{\mathbf{k}}) = \left[\mathbf{Z}(\vec{\mathbf{k}})\right]^* \mathbf{H}^L \mathbf{Z}(\vec{\mathbf{k}}). \tag{A.71}$$

Note that we would have obtained the same result (eq. A.69) if we had used eq. (A.65) rather than eq. (A.66).

We derive the initial conditions for eq. (A.69). Note that eq. (A.48) is written as

$$\boldsymbol{\psi}^{(N_x,N_y)}(t;\vec{\mathbf{k}}) = \mathbf{Z}(\vec{\mathbf{k}})\widetilde{\boldsymbol{\psi}}^{(0,0)}(t;\vec{\mathbf{k}})\exp(\mathrm{i}k_x hN_x + \mathrm{i}k_y hN_y), \tag{A.72}$$

where $\widetilde{\boldsymbol{\psi}}^{(0,0)}(t;\vec{\mathbf{k}})$ is a vector whose $2n^2$ elements are

$$\left[\widetilde{\boldsymbol{\psi}}^{(0,0)}(t;\vec{\mathbf{k}})\right]_{(\alpha,p_x,p_y)} = \left[\boldsymbol{\psi}^{(0,0)}(t;\vec{\mathbf{k}})\right]_{(\alpha,p_x,p_y)}, \tag{A.73}$$

with $p_x, p_y = 0, \ldots, n-1$. Comparing eq. (A.66) with eq. (A.72), and using eqs. (A.56) and (A.57), the initial conditions for eq. (A.69) are

$$\mathbf{v}(0;\vec{\mathbf{k}}) = \widetilde{\boldsymbol{\psi}}^{(0,0)}(0;\vec{\mathbf{k}}) \tag{A.74}$$

$$\dot{\mathbf{v}}(0;\vec{\mathbf{k}}) = \dot{\widetilde{\boldsymbol{\psi}}}^{(0,0)}(0;\vec{\mathbf{k}}). \tag{A.75}$$

We numerically solve the $2n^2$ simultaneous differential equations, eq. (A.69), with the initial conditions eqs. (A.74) and (A.75). To do this, we write the solution by representing it in terms of an eigenfunction expansion:

$$\mathbf{v}(t;\vec{\mathbf{k}}) = \sum_{p=1}^{2n^2} a_p(t;\vec{\mathbf{k}})\mathbf{c}_p(\vec{\mathbf{k}}), \tag{A.76}$$

where each $\mathbf{c}_p(\vec{\mathbf{k}})$ is an eigenvector of the following eigenvalue problem with eigen-

frequency $\Lambda_p(\vec{\mathbf{k}})$:

$$\left\{ \left[\Lambda_p(\vec{\mathbf{k}}) \right]^2 \widetilde{\mathbf{T}}(\vec{\mathbf{k}}) - \widetilde{\mathbf{H}}(\vec{\mathbf{k}}) \right\} \mathbf{c}_p(\vec{\mathbf{k}}) = 0. \tag{A.77}$$

The othonormalization of the eigenvectors is given by:

$$\left[\mathbf{c}_q(\vec{\mathbf{k}}) \right]^* \widetilde{\mathbf{H}}(\vec{\mathbf{k}}) \mathbf{c}_p(\vec{\mathbf{k}}) = \left[\Lambda_p(\vec{\mathbf{k}}) \right]^2 \left[\mathbf{c}_q(\vec{\mathbf{k}}) \right]^* \widetilde{\mathbf{T}}(\vec{\mathbf{k}}) \mathbf{c}_p(\vec{\mathbf{k}}) = \delta_{pq} \quad \text{for} \quad p, q = 1, \ldots, 2n^2. \tag{A.78}$$

Substituting eq. (A.76) into eq. (A.69) with the initial conditions eqs. (A.74) and (A.75) the expansion coefficients $a_p(t; \vec{\mathbf{k}})$ are found to be:

$$a_p(t; \vec{\mathbf{k}}) = \left[\mathbf{c}_p(\vec{\mathbf{k}}) \right]^* \widetilde{\mathbf{T}}(\vec{\mathbf{k}}) \left\{ \widetilde{\boldsymbol{\psi}}^{(0,0)}(0; \vec{\mathbf{k}}) \cos \left[\Lambda_p(\vec{\mathbf{k}}) t \right] + \dot{\widetilde{\boldsymbol{\psi}}}^{(0,0)}(0; \vec{\mathbf{k}}) \frac{\sin \left[\Lambda_p(\vec{\mathbf{k}}) t \right]}{\Lambda_p(\vec{\mathbf{k}})} \right\}. \tag{A.79}$$

We define the relative error of the wavefield computed using the SEM operators for a particular time t as follows:

$$\begin{aligned} \text{Relative Error} &= \frac{\sqrt{\sum_{N_x, N_y} \left| \mathbf{d}^{(N_x, N_y)}(t; \vec{\mathbf{k}}) - \boldsymbol{\psi}^{(N_x, N_y)}(t; \vec{\mathbf{k}}) \right|^2}}{\sqrt{\sum_{N_x, N_y} \left| \boldsymbol{\psi}^{(N_x, N_y)}(t; \vec{\mathbf{k}}) \right|^2}} \\ &= \frac{\left| \mathbf{v}(t; \vec{\mathbf{k}}) - \widetilde{\boldsymbol{\psi}}^{(0,0)}(t; \vec{\mathbf{k}}) \right|}{\left| \widetilde{\boldsymbol{\psi}}^{(0,0)}(t; \vec{\mathbf{k}}) \right|}, \end{aligned} \tag{A.80}$$

where the argument $\vec{\mathbf{k}}$ of $\mathbf{d}^{(N_x, N_y)}(t; \vec{\mathbf{k}})$ indicates the wavenumber vector of the plane wave used in the initial conditions, eqs. (A.56) and (A.57).

We also estimate the grid dispersion as follows:

$$\text{Grid Dispersion} = \frac{\left| \Lambda_{p'}(\vec{\mathbf{k}}) - c|\vec{\mathbf{k}}| \right|}{c|\vec{\mathbf{k}}|}, \tag{A.81}$$

where p' is selected to minimize the error of the eigenfunctions defined as:

$$\min_{p=1,\ldots,2n^2} \frac{\left|\mathbf{c}_p(\vec{\mathbf{k}}) - \widetilde{\boldsymbol{\psi}}^{(0,0)}(0;\vec{\mathbf{k}})\right|}{\left|\widetilde{\boldsymbol{\psi}}^{(0,0)}(0;\vec{\mathbf{k}})\right|}. \tag{A.82}$$

This definition is essentially same as in previous studies of dispersion analysis (e.g., Mulder 1999). Note that this definition assumes that the numerical solution, eq. (A.76) will approximately satisfy

$$\mathbf{v}(t;\vec{\mathbf{k}}) \approx \mathbf{c}_{p'}(\vec{\mathbf{k}}) \exp\left(\mathrm{i}\Lambda_{p'}(\vec{\mathbf{k}})t\right) \approx \widetilde{\boldsymbol{\psi}}^{(0,0)}(0;\vec{\mathbf{k}}) \exp\left(\mathrm{i}\Lambda_{p'}(\vec{\mathbf{k}})t\right), \tag{A.83}$$

and that the effects of other modes with $p \neq p'$, which are so-called "spurious modes," will be small. In other words, it implies that the numerical solution still approximately propagates as a harmonic wave with the numerical phase velocity changing in accordance with the dispersion curve.

A.2.4 Finding degenerate cases

We show below that it is straightforward to search systematically for degenerate cases. Let us consider two waves, with the same frequency ω but with different wavenumber vectors $\vec{\mathbf{k}}$ and $\vec{\mathbf{k}}'$. The operators for coupling between harmonic plane waves with different wavenumbers will be zero:

$$\sum_{N_x=-\infty}^{\infty} \sum_{N_y=-\infty}^{\infty} \left[\boldsymbol{\psi}^{(N_x,N_y)}(t;\vec{\mathbf{k}}')\right]^* \mathbf{T}^L \boldsymbol{\psi}^{(N_x,N_y)}(t;\vec{\mathbf{k}}) = 0 \tag{A.84}$$

$$\sum_{N_x=-\infty}^{\infty}\sum_{N_y=-\infty}^{\infty}\left[\boldsymbol{\psi}^{(N_x,N_y)}(t;\vec{\mathbf{k}}')\right]^{*}\mathbf{H}^{L}\boldsymbol{\psi}^{(N_x,N_y)}(t;\vec{\mathbf{k}})=0, \tag{A.85}$$

unless the following two conditions are satisfied:

$$k_x' = k_x + 2\pi M_x/h \tag{A.86}$$

$$k_y' = k_y + 2\pi M_y/h, \tag{A.87}$$

where M_x and M_y are integers, in which case degenerate coupling will occur. Eqs. (A.86) and (A.87) hold not only for cases when both of the waves are P-waves, or S-waves, but also for cases where one wave is a P-wave and the other is a S-wave. In the next subsection we present numerical examples showing that waves with the same frequency but different wavenumbers can be excited as artifacts when eqs. (A.86) and (A.87) hold.

To find degenerate cases we parameterize $\vec{\mathbf{k}}$ and $\vec{\mathbf{k}}'$ as follows:

$$\vec{\mathbf{k}} = (k_x, k_y) = k(\cos\theta, \sin\theta), \quad \vec{\mathbf{k}}' = (k_x', k_y') = k'(\cos\theta', \sin\theta'). \tag{A.88}$$

Since the dispersion relation for the 2-D isotropic case is given by eq. (A.53), from eqs. (A.86) and (A.87) ω and ω' for a degenerate case can be written in terms of k and θ as follows:

$$\omega = ck \tag{A.89}$$

$$\omega' = c'\sqrt{(k\cos\theta + 2\pi M_x/h)^2 + (k\sin\theta + 2\pi M_y/h)^2}. \tag{A.90}$$

where c and c' are the phase velocities of the first and second waves, respectively.

Hereafter, k (and k') are normalized as

$$\widetilde{k} = \frac{kh}{2\pi n}, \tag{A.91}$$

which corresponds to the spatial sampling rate (e.g., De Basabe & Sen 2007; Seriani & Oliveira 2008a, b), and ω (and ω') are normalized as

$$\widetilde{\omega} = \frac{\omega h}{2\pi n}. \tag{A.92}$$

Figs. A.2a-d show degenerate coupling points predicted from intersections of eqs. (A.89) and (A.90) with various M_x and M_y, for $\theta = 0°$, $15°$, $30°$, and $45°$. We use $n = 4$, and the P-wave to S-wave velocity ratio

$$r = V_P/V_S = \sqrt{3}. \tag{A.93}$$

We show the results in the range $\widetilde{k}' \leq 0.2$, which is the range shown by previous studies (e.g., De Basabe & Sen 2007; Seriani & Oliveira 2008a, b). The solid lines and dashed curves show eqs. (A.89) and eq. (A.90), respectively. The red and blue colors correspond to P- and S-waves, respectively. The intersections between solid and dashed lines indicate degenerate coupling points. Table A.1 shows the values of $(\widetilde{k}, \theta)$ and $(\widetilde{k}', \theta')$ at the intersections; the intersections are labeled P01–27 in Table A.1. The second column of Table A.1 indicates the panel of Fig. A.2 in which the degenerate point is located. Note that P24 and P27 have two entries each in Table A.1 because they represent triple intersections. The colors of the

intersecting lines in the various panels of Fig. A.2 indicate the types of coupling: e.g., P08 corresponds to P-P coupling, P09 to P-S coupling, P14 to S-P coupling, and P15 to S-S coupling.

A.2.5 Numerical Results

To show the essence of the effects of degeneracy, we first consider SEM with $n = 4$ for the scalar wave equation. The other problem settings for the numerical experiment are same as those stated above. Since the above theoretical results can be straightforwardly simplified to apply to the scalar wave equation, we omit a detailed derivation. Note that since only P-waves are excited for the acoustic case, degenerate coupling can occur only at the values of the intersections between the red solid and red dashed lines in Fig. A.2.

Fig. A.3 shows the relative error of the solution, eq. (A.80), for cases when harmonic scalar waves are input as the initial conditions, where the frequencies and the wavenumbers of the input waves are along the red solid lines of Fig. A.2. For the unit of time t, we use the period of the input wave

$$T = 2\pi/\omega = 2\pi/(ck). \tag{A.94}$$

We see peaks of the error in Fig. A.3 at the wavenumbers labeled as corresponding to the values of P01, P08, P16, and P24 in Table A.1. Fig. A.4 show an enlargement of Fig. A.3b focusing around peak P08. In the vicinity of the peak, the error becomes increasingly large as time passes. Figs. A.5 show the grid dispersion, eq. (A.81). The dispersion curves in Figs. A.5 show localized large errors at the same wavenumbers

as the peaks in Figs. A.3, labeled by the same numbering. The theoretical reason for the localized errors in Figs. A.3–A.5 is degenerate coupling, as shown in Section A.1.

Hereafter we consider examples for the elastic wave equation. Note that in the elastic cases, the upper limit of the spatial sampling rate is determined by S-waves, because the wavelength of S-waves is always smaller than that of P-waves with the same frequencies. However, for simplicity, as the abscissa of the graphs below we use the wavenumber of the input waves normalized using eq. (A.91) rather than by the corresponding S-wavenumber. This definition is same as other previous error analyses (e.g., De Basabe & Sen 2007; Seriani & Oliveira 2008a, b; Moczo *et al.* 2011).

In Figs. A.6–A.8, we use $n = 4$ and $r = \sqrt{3}$, which are the same values of the parameters used in Fig. A.2 and Table A.1. Figs. A.6 show the relative error of the solution, eq. (A.80), with $t = 100T$, for cases when P-waves and S-waves are input as the initial conditions, respectively, where the frequencies and the wavenumbers of the input waves are along the solid lines of Figs. A.2. Figs. A.7 show the grid dispersion for P and S-waves computed by eq. (A.81). We see peaks of the error of the numerical solution labeled P01, P05, P08, P09, P14, P15, P16, P18, P19, P25, and P27 in Figs. A.6, each of which corresponds to an intersection of the curves in Figs. A.2, and to the row with the same labelling in Table A.1. Comparing Figs. A.6 with Figs. A.3, we see additional peaks caused by P-S and S-P coupling. Although we confirmed that all of the peaks in Figs. A.3–A.7 correspond to entries in Table A.1, the strength of the degenerate coupling effects appears to depend on the detailed properties of the SEM operators.

In Fig. A.8, we show snapshots of the displacement field at $t = 100T$ when we input S-waves with $\theta = 15^\circ$ and $\widetilde{k} = 0.165$, 0.169 (P14 in Table A.1), and 0.175, respectively. We use Legendre-Lagrange interpolation to calculate the displacements at intermediate points between the GLL node points. A movie of the wave propagation simulations is available online as supplementary material in Hasegawa *et al.* (2016). We see in the movie that when $\widetilde{k} = 0.165$ or 0.175, the waves seem to propagate accurately. On the other hand, we see that when $\widetilde{k} = 0.169$ the wavefield is contaminated by artificial coupling with the degenerate P-wave with $\theta = 153^\circ$ and $\widetilde{k} = 0.097$ (see P14 in Table A.1). The artificial excitation of the P-wave can be seen in the bottom panel of Figs. A.8b for the longitudinal component. (Note that the longitudinal component is amplified tenfold.)

Figs. A.9 show the relative error of the solution at $t = 100T$ for various P-wave to S-wave velocity ratios r with fixed polynomial order $n = 4$. The green, blue, and red lines correspond to the error for $r = 6$, $r = 3$, and $r = \sqrt{3}$, respectively. The solid and dashed lines correspond to the error for input P-waves and S-waves, respectively. Although the strength of the degenerate coupling effects depends heavily on the detailed properties of the SEM operators, we see that the number of peaks of the error increases for larger r, especially for cases when P-waves are input. This is because the slopes of the red solid lines in Figs. A.2 become steeper for larger values of r, and thus within $\widetilde{k} \leq 0.2$, the red solid lines have more opportunities to intersect with the blue dashed lines.

Fig. A.10 shows the relative error of the solution at $t = 100T$ for various polynomial orders n with fixed P-wave to S-wave velocity ratio $r = \sqrt{3}$. The green, blue,

and red lines correspond to the error for $n = 1$, $n = 4$, and $n = 8$, respectively. The solid and dashed lines correspond to the error for input P-waves and S-waves, respectively. Note that SEM for $n = 1$ is equivalent to the classical finite difference method. In the cases for $n = 1$, (k'_x, k'_y) of eqs. (A.86) and (A.87) is always outside the physically meaningful range, eq. (A.58).

A.3 Discussion

In Appendix A we used the methods of GT95 to conduct a general error analysis of ho-FEMs for solving the elastic equation of motion. We showed that degeneracy (coupling between modes with identical or nearly identical frequencies) can cause artificial excitation of other modes in the synthetic seismograms unless the eigenvectors of the exact problem are also eigenvectors of the numerical operators, which in general will not be the case.

In Section A.2 we confirmed the existence of errors due to degenerate coupling by a simple numerical experiment. Some previous studies have noted the presence of such errors in synthetic seismograms computed by ho-FEMs for the 1-D Helmholtz equation. Thompson & Pinsky (1994) and Mulder (1999) showed the existence of what they called aliasing errors, which occur when an integer multiple of the wavelength coincides with the element length. Such errors are particular examples of errors that occur because of degenerate coupling between modes.

Our numerical example in Section A.2 is for SEM, but it should be easy to make similar tests for other higher-order numerical methods for homogeneous and isotropic models. As shown in Section A.1, the strength of the degenerate coupling

effects mainly depend on the individual properties of the numerical mass and stiffness matrices. Therefore to simplify the problem settings, we do not consider the effects of temporal discretization on time evolution. Although the absolute values of the figures in this study will change depending on the temporal discretization, the basic character of the figures will not change.

In this study we do not consider the case of a viscoelastic medium, for which the effects of degeneracy might become smaller because of existence of the imaginary parts of the eigenfrequencies. This is an important subject for future work.

It seems reasonable that errors due to degenerate coupling should also occur for applications of ho-FEMs to heterogeneous models. but it seems hard to predict what the systematics of such errors would be.

Finally, in closing for this section, we attempt to provide a non-technical explanation of our results. The results presented in Appendix A do not suggest that the error of numerical solutions computed by ho-FEMs are large in general, notwithstanding their small numerical dispersion. What we are saying is that synthetics computed using ho-FEMs are subject to significant degradation from their general level of accuracy for particular frequency-wavenumber combinations where degenerate coupling occurs. We have presented theoretical derivations to show why this occurs, and the phenomenon is ubiquitous in the numerical examples we presented for homogeneous cases. These results should not be a surprise, because they are a natural generalization of Mulder's (1999) results for a 1-D case. On the other hand, informal conversations with users of ho-FEMs suggest that such "pinpoint errors" have not been noticed as a problem in practical applications (although it also ap-

pears that no one has systematically investigated their possible existence). Users of ho-FEMs should consider the possibility that the effects of degenerate coupling may be degrading the accuracy of their results when choosing the size of the cells used in their grids.

Table A.1: Degenerate coupling points

		target wave					degenerate wave					
	Panel	wave-type	$\widetilde{k}$	θ	$\widetilde{k}_x$	$\widetilde{k}_y$	wave-type	$\widetilde{k}'$	θ'	$\widetilde{k}'_x$	$\widetilde{k}'_y$	M_x	M_y
P01	a	P	0.125	0°	0.125	0.000	P	0.125	180°	-0.125	0.000	-1	0
P02	a	P	0.092	0°	0.092	0.000	S	0.158	180°	-0.158	0.000	-1	0
P03	a	P	0.155	0°	0.155	0.000	S	0.268	111°	-0.095	0.250	-1	1
P04	a	P	0.177	0°	0.177	0.000	S	0.306	55°	0.177	0.250	0	1
P05	a	P	0.183	0°	0.183	0.000	S	0.317	180°	-0.317	0.000	-2	0
P06	a	S	0.159	0°	0.159	0.000	P	0.092	180°	-0.092	0.000	-1	0
P07	a	S	0.125	0°	0.125	0.000	S	0.125	180°	-0.125	0.000	-1	0
P08	b	P	0.129	15°	0.125	0.034	P	0.129	165°	-0.125	0.034	-1	0
P09	b	P	0.093	15°	0.090	0.024	S	0.162	171°	-0.160	0.024	-1	0
P10	b	P	0.140	15°	0.135	0.036	S	0.243	-118°	-0.115	-0.214	-1	-1
P11	b	P	0.147	15°	0.142	0.038	S	0.255	-56°	0.142	-0.212	0	-1
P12	b	P	0.177	15°	0.171	0.046	S	0.306	105°	-0.079	0.296	-1	1
P13	b	P	0.187	15°	0.180	0.048	S	0.323	171°	-0.320	0.048	-2	0
P14	b	S	0.169	15°	0.163	0.044	P	0.097	153°	-0.087	0.044	-1	0
P15	b	S	0.129	15°	0.125	0.034	S	0.129	165°	-0.125	0.034	-1	0
P16	c	P	0.144	30°	0.125	0.072	P	0.144	150°	-0.125	0.072	-1	0
P17	c	P	0.183	30°	0.159	0.092	P	0.183	-120°	-0.092	-0.159	-1	-1
P18	c	P	0.099	30°	0.089	0.050	S	0.171	163°	-0.164	0.050	-1	0
P19	c	P	0.125	30°	0.108	0.063	S	0.217	-60°	0.108	-0.187	0	-1
P20	c	P	0.132	30°	0.114	0.066	S	0.229	-126°	-0.136	-0.184	-1	-1
P21	c	P	0.198	30°	0.172	0.099	S	0.343	163°	-0.328	0.099	-2	0
P22	c	S	0.144	30°	0.125	0.072	S	0.144	150°	-0.125	0.072	-1	0
P23	c	S	0.183	30°	0.159	0.091	S	0.183	-120°	-0.091	-0.159	-1	-1
P24	d	P	0.177	45°	0.125	0.125	P	0.177	-135°	-0.125	-0.125	-1	-1
P24	d	P	0.177	45°	0.125	0.125	P	0.177	-45°	0.125	-0.125	0	-1
P25	d	P	0.109	45°	0.077	0.077	S	0.189	-66°	0.077	-0.173	0	-1
P26	d	P	0.130	45°	0.092	0.092	S	0.224	-135°	-0.158	-0.158	-1	-1
P27	d	S	0.177	45°	0.125	0.125	S	0.177	-135°	-0.125	-0.125	-1	-1
P27	d	S	0.177	45°	0.125	0.125	S	0.177	-45°	0.125	-0.125	0	-1

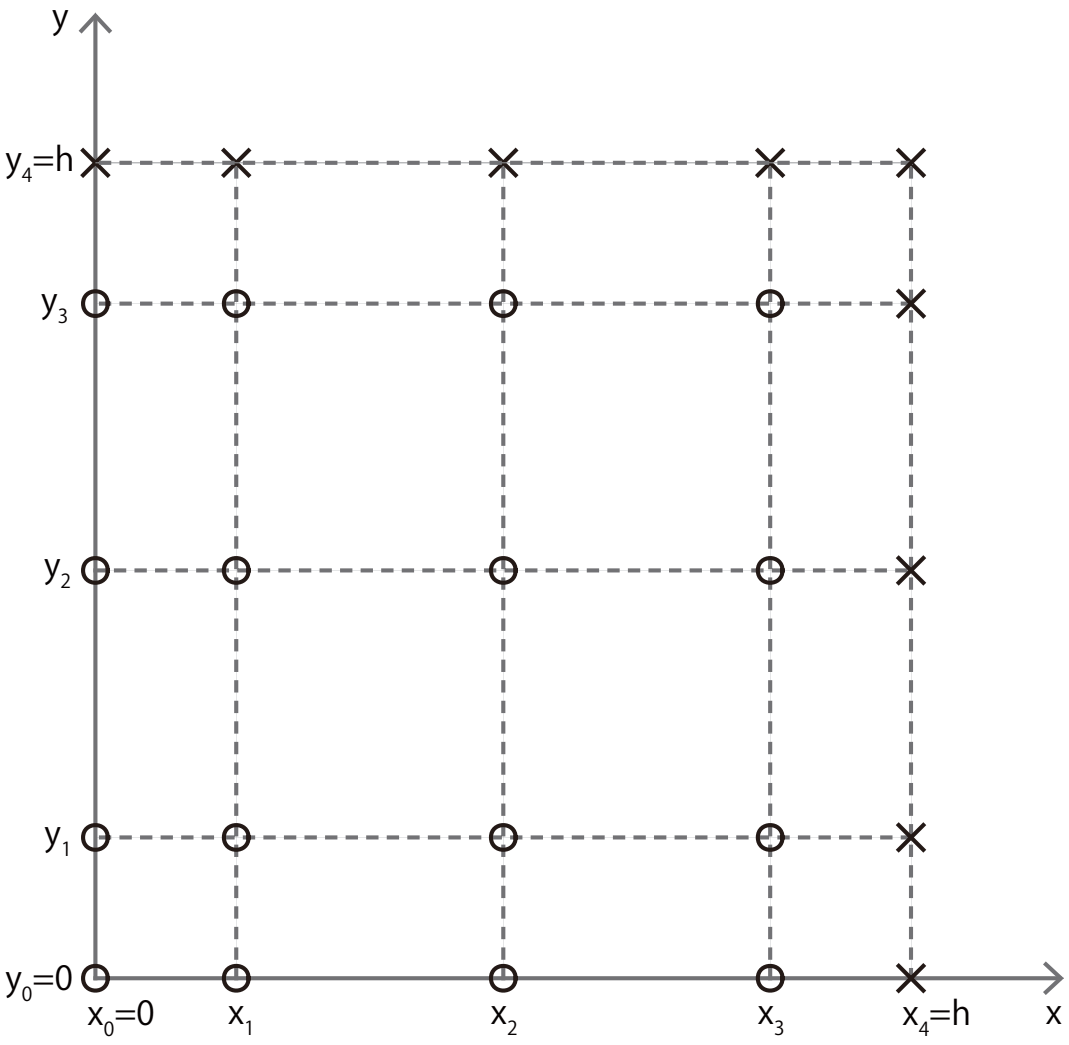

Figure A.1: The GLL nodes of a cell for $n = 4$. The circles indicate linearly independent nodes, and the crosses indicate nodes which are linearly dependent due to the boundary conditions in eqs. (A.60) and (A.61).

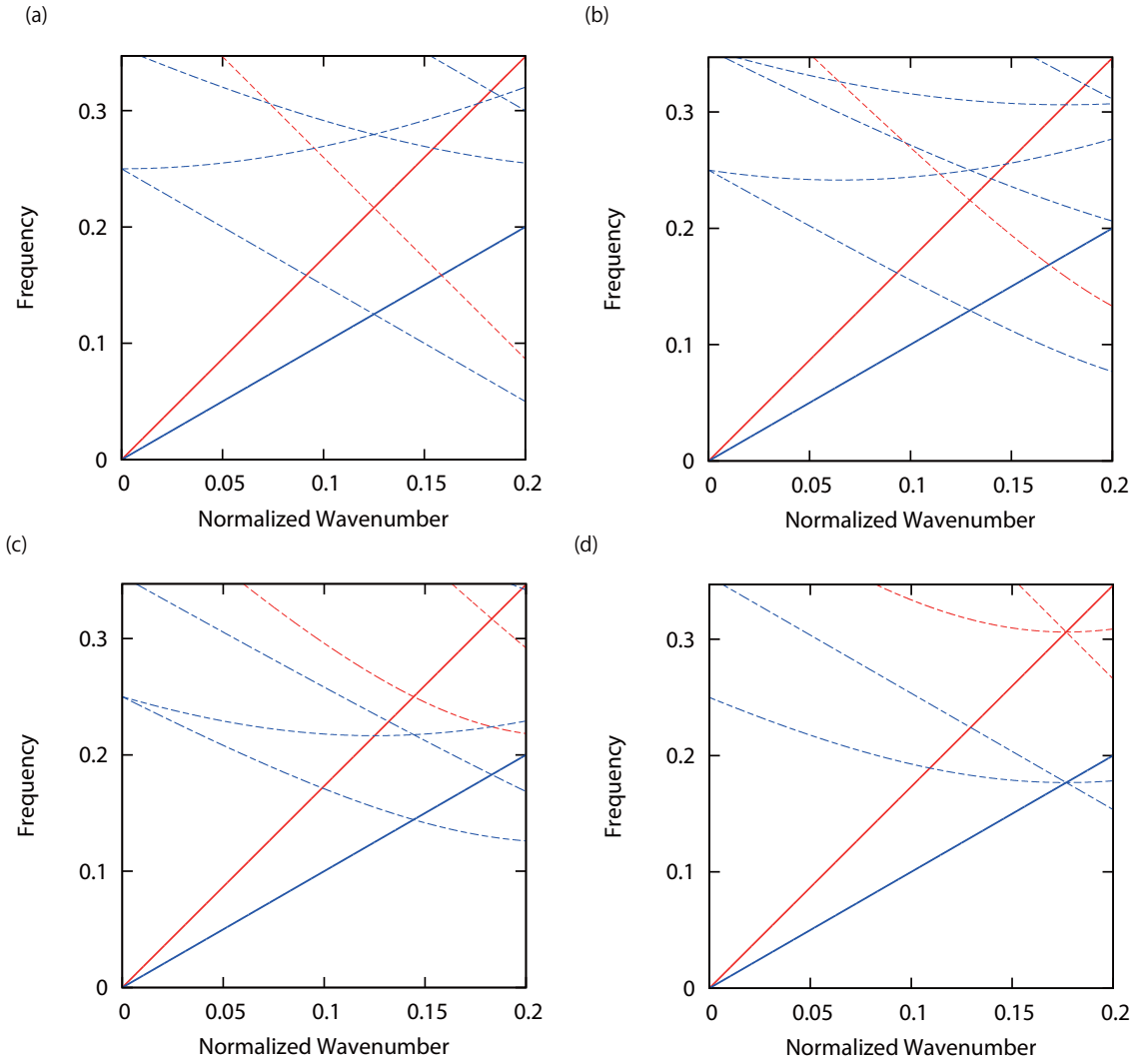

Figure A.2: Degenerate coupling points predicted using eqs. (A.89) and (A.90) for various values of M_x and M_y. We use $n = 4$, and $r = V_P/V_S = \sqrt{3}$. The solid lines show the values of eq. (A.89) as functions of the normalized wavenumber $\widetilde{k}$ as defined in eq. (A.91) The red and blue colors correspond to P-waves and S-waves, respectively. The dashed red and blue curves correspond to eq. (A.90) as functions of $\widetilde{k}$ for P-waves and S-waves, respectively, for various M_x and M_y. The intersections between the solid lines and dashed curves indicate degenerate coupling points. ω is normalized using eq. (A.92). Panels a, b, c, and d are for incidence angles of $\theta = 0°$, $15°$, $30°$, and $45°$, respectively. See Table A.1 for details of degenerate coupling points.

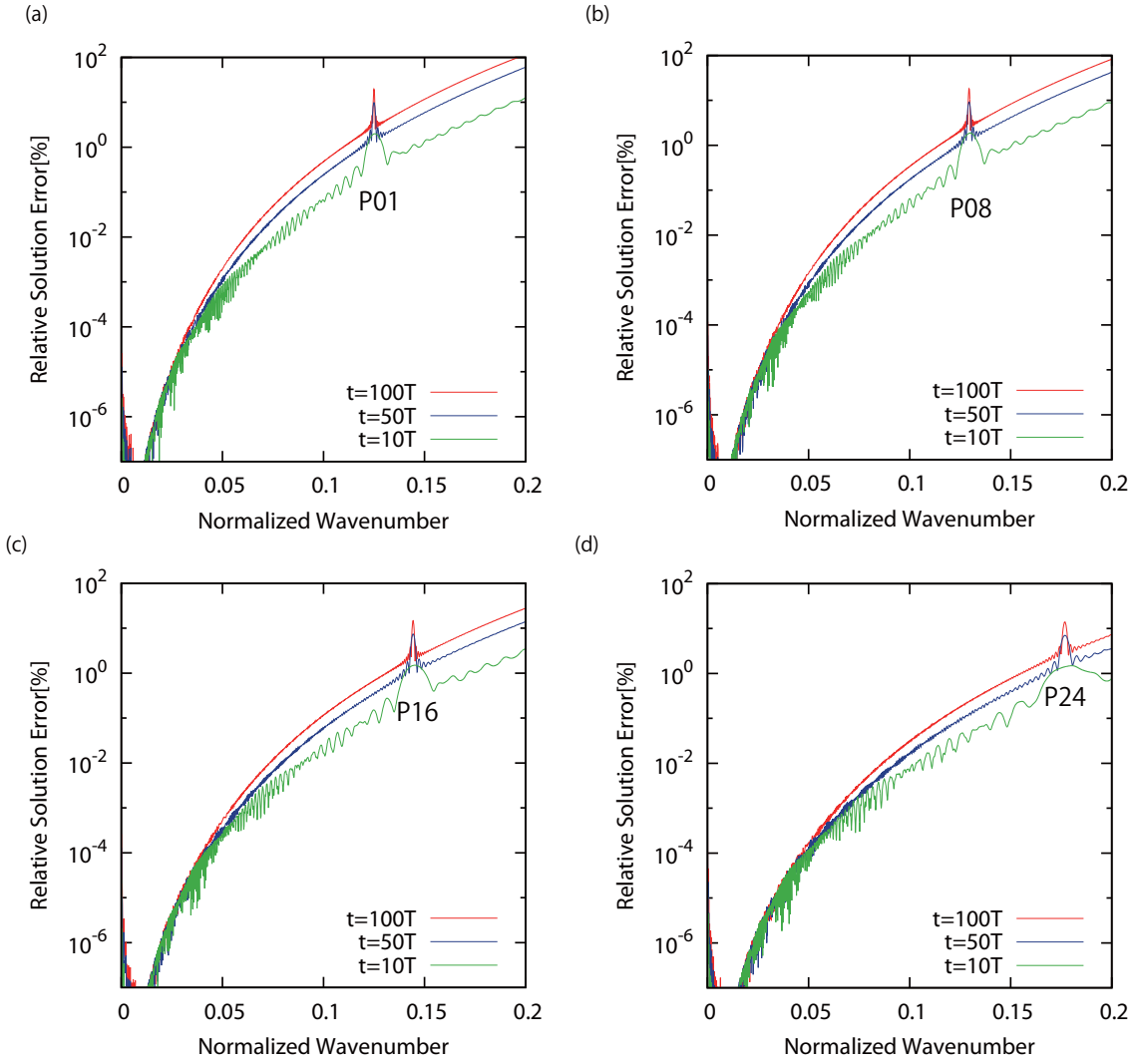

Figure A.3: The relative solution error for the scalar wave equation as given by eq. (A.80), when the frequencies and the wavenumbers of the input wave at $t = 0$ are along the red solid lines of Figs. A.2. We consider SEM with $n = 4$. We use the period T of the input wave, eq. (A.94), as the unit of time t. Panels a, b, c, and d are for propagation angles of the input wave of $\theta = 0°$, $15°$, $30°$, and $45°$, respectively.

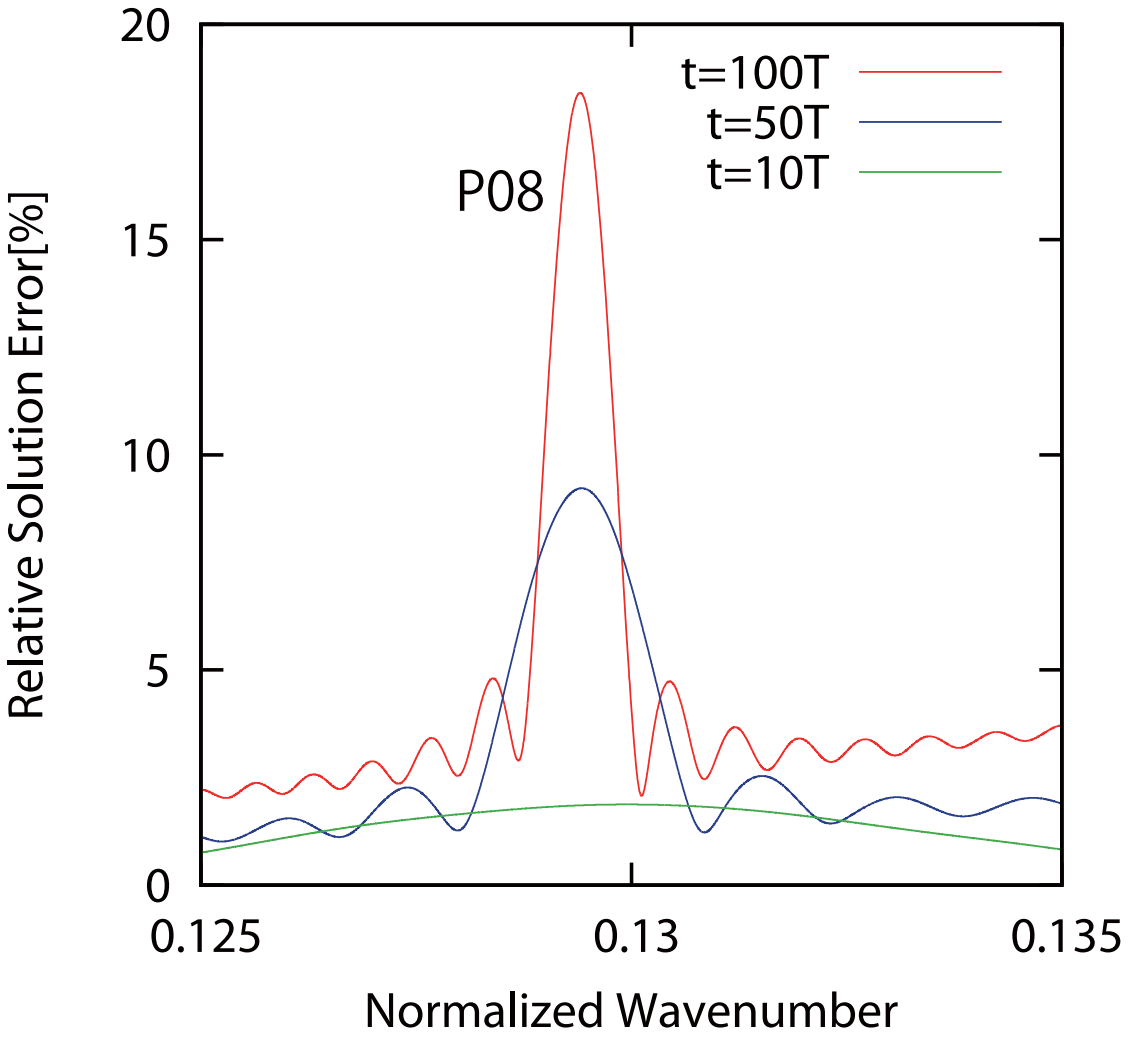

Figure A.4: The same as Fig. A.3b in the vicinity of Peak P08 only.

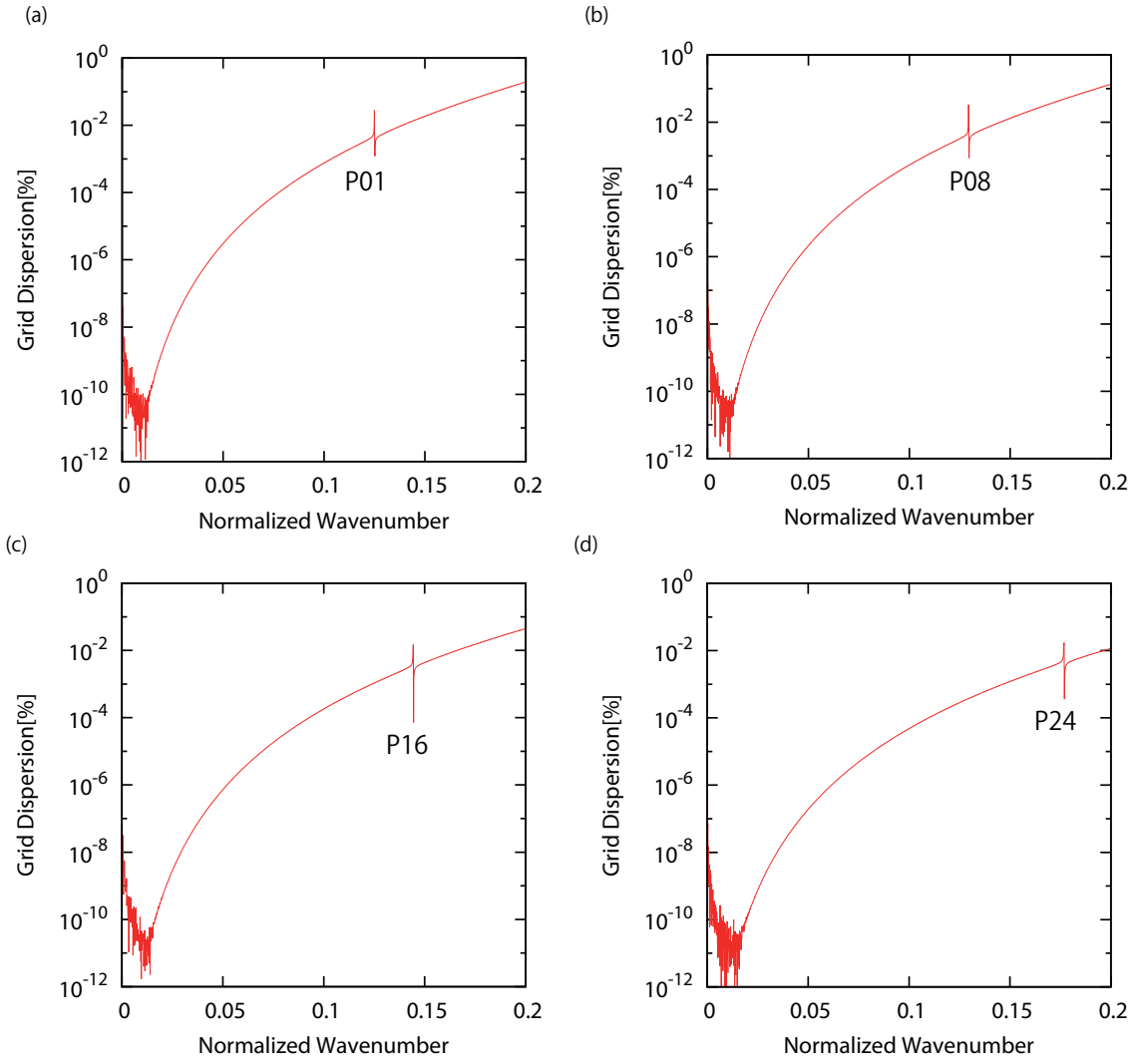

Figure A.5: The grid dispersion for the scalar wave equation as given by eq. (A.81). We consider SEM with $n = 4$. Panels a, b, c, and d are for angles of the wavenumber vector $\theta = 0°$, $15°$, $30°$, and $45°$, respectively.

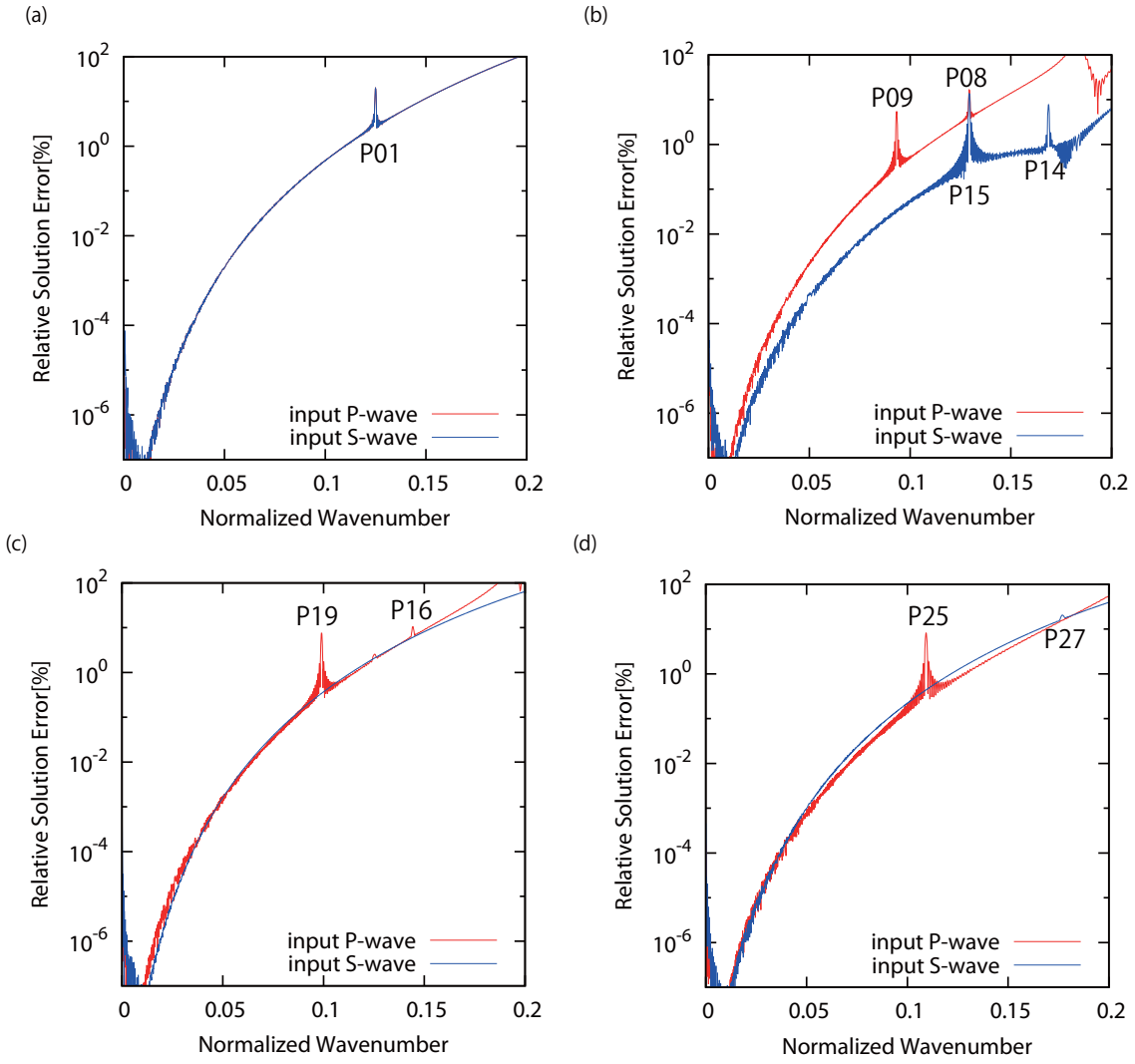

Figure A.6: The relative solution error for the elastic wave equation as given by eq. (A.80), when the frequencies and the wavenumbers of the input wave at $t = 0$ are along the solid lines of Fig. A.2 We consider SEM with $n = 4$, and $r = \sqrt{3}$. We use the period T of the input wave, eq. (A.94), as the unit of time t. Panels a, b, c, and d are for propagation angles of the input wave of $\theta = 0°$, $15°$, $30°$, and $45°$, respectively. The red and blue lines are for input P and S-waves, respectively.

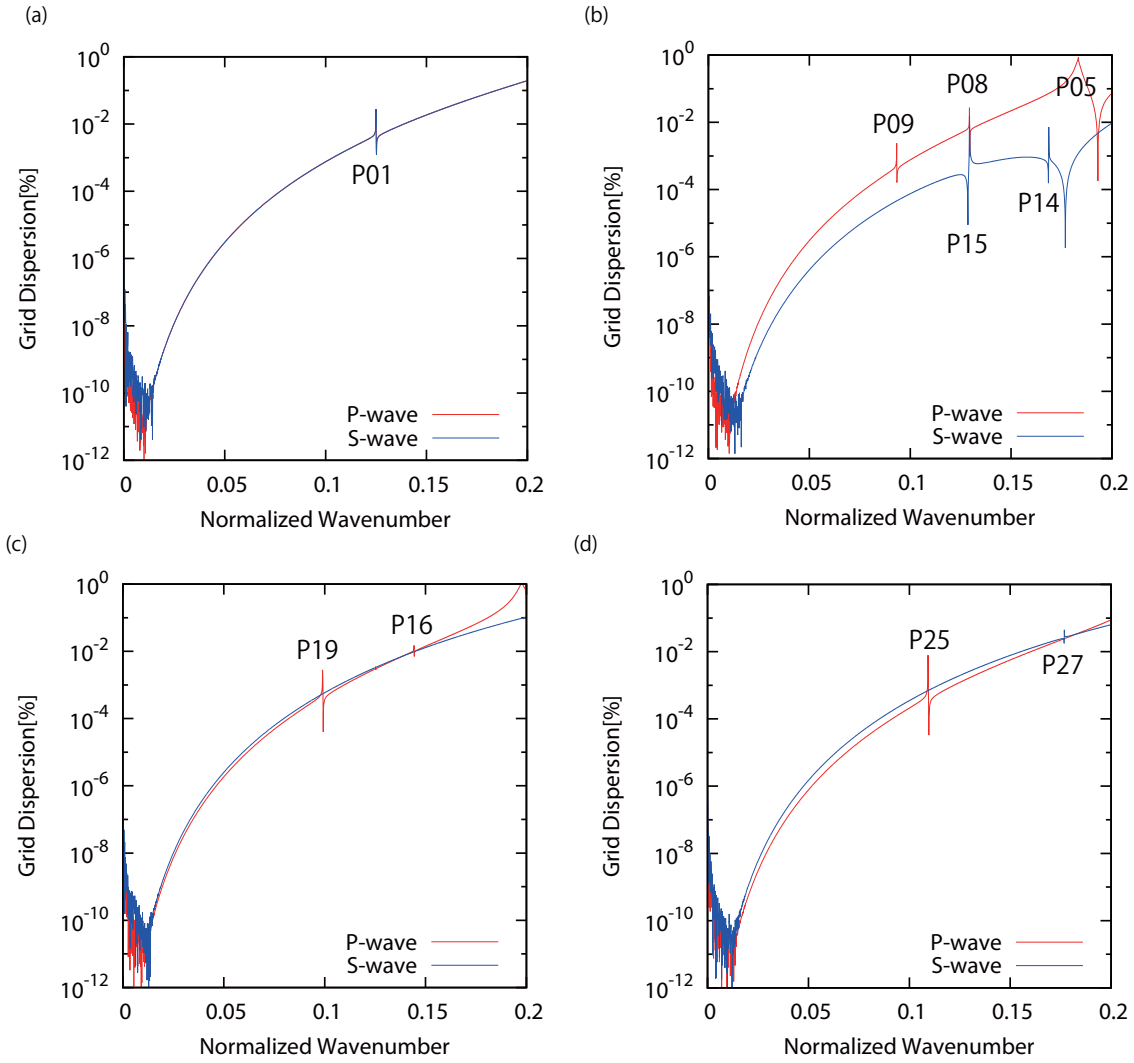

Figure A.7: The grid dispersion for the elastic wave equation as given by eq. (A.81). We consider SEM with $n = 4$, and $r = \sqrt{3}$. Panels a, b, c, and d are for angles of the wavenumber vector of $\theta = 0°$, $15°$, $30°$, and $45°$, respectively. The red and blue lines for the P and S-waves, respectively.

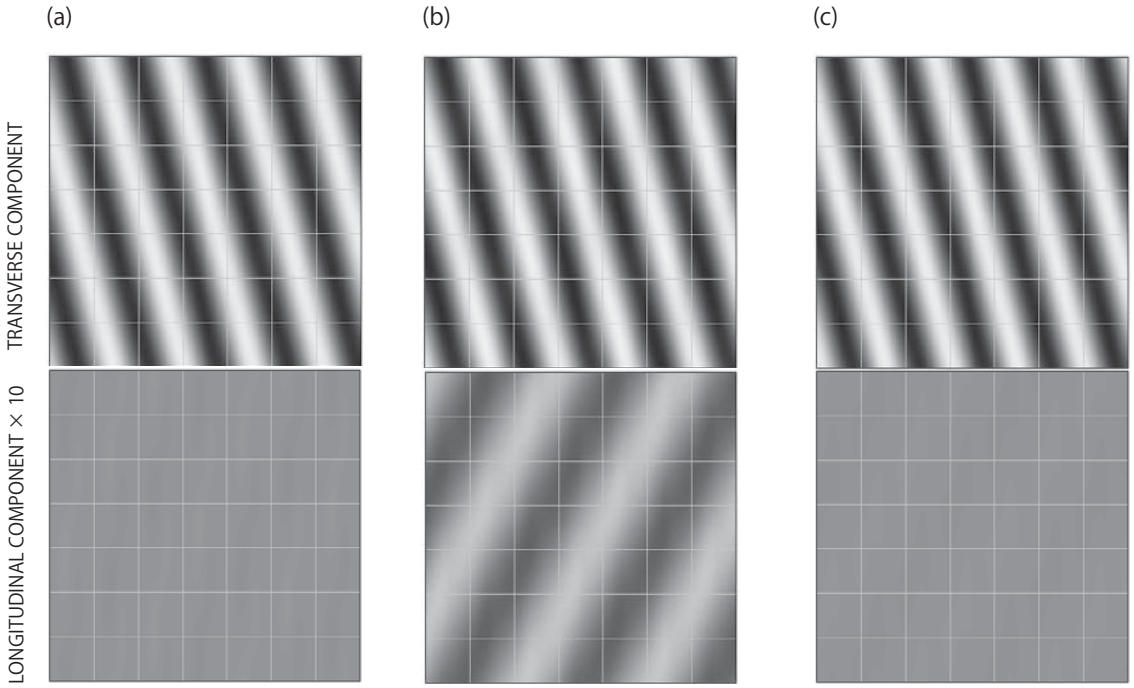

Figure A.8: Snapshots of the numerical displacement fields at $t = 100T$ computed by SEM with $n = 4$ when we input S-waves with $\theta = 15^\circ$ and (a) $k = 0.165$, (b) $k = 0.169$, and (c) $k = 0.175$, respectively. We use Legendre-Lagrange interpolation to compute the displacement at intermediate points between the GLL nodes: (top panels) the transverse (perpendicular to the wavenumber vector) component of the displacement fields, (bottom panels) the longitudinal (parallel to the wavenumber vector) component of the displacement fields. Note that the longitudinal component is amplified tenfold.

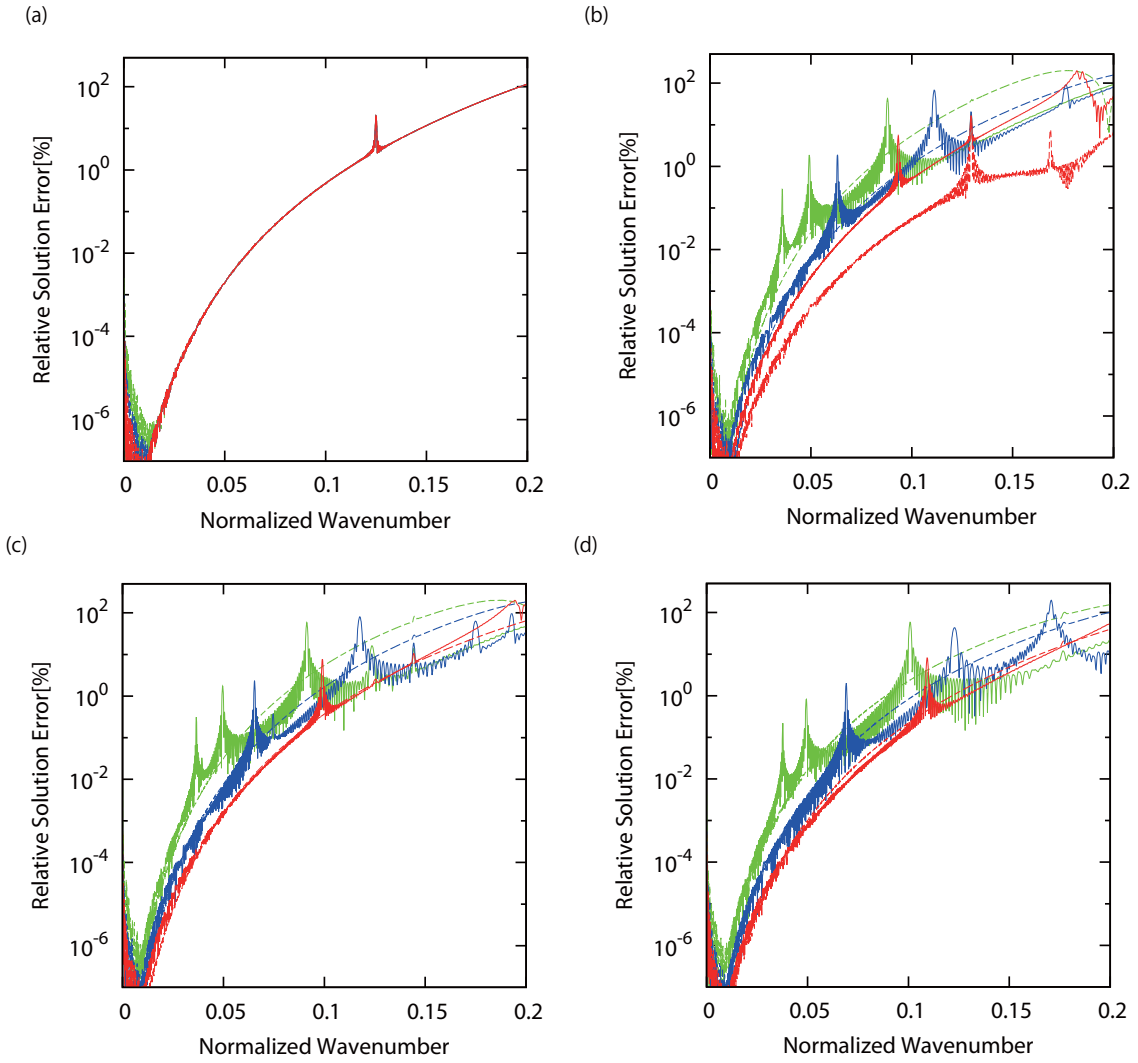

Figure A.9: The relative solution error for the elastic wave equation as given by eq. (A.80). We consider SEM with $n = 4$. We use the period T of the input wave, eq. (A.94), as the unit of time t. Panels a, b, c, and d are for propagation angles of the input wave of $\theta = 0°$, $15°$, $30°$, and $45°$, respectively. The solid and green lines are for input P and S-waves, respectively. The green, blue, and red lines are for $r = \sqrt{3}$, 3, and 6, respectively. As only some of the peaks in this figure correspond to Table A.1, none are labelled.

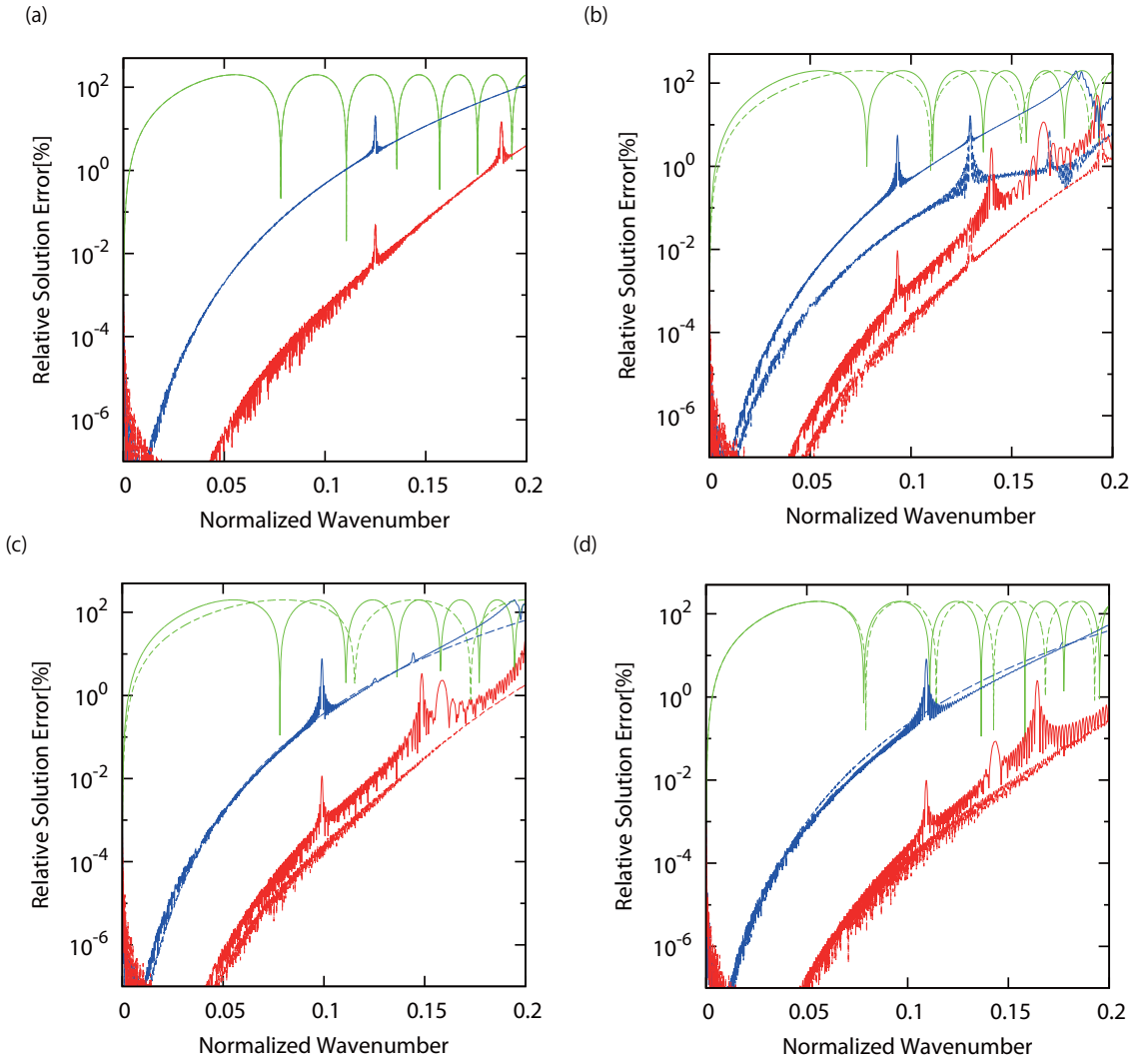

Figure A.10: The relative solution error for the elastic wave equation as given by eq. (A.80). We consider $r = \sqrt{3}$. We use the period T of the input wave, eq. (A.90), as the unit of time t. Panels a, b, c, and d are for propagation angles of the input wave of $\theta = 0°$, $15°$, $30°$, and $45°$, respectively. The solid and green lines are for the input P and S-waves, respectively. The green, blue, and red lines are for SEM with $n = 1$, 4, and 8, respectively. Note that SEM with $n = 1$ is equivalent to the classical finite difference method. As only some of the peaks in this figure correspond to Table A.1, none are labelled.

Appendix B

本付録（173 から 187 ページ）については、5 年以内に雑誌等で刊行予定のため、非公開。